



Origin of the early Permian Wajilitag igneous complex and associated Fe–Ti oxide mineralization in the Tarim large igneous province, NW China



Jun Cao ^{a,c}, Christina Yan Wang ^b, Chang-Ming Xing ^{b,c}, Yi-Gang Xu ^{a,*}

^a State Key Laboratory of Isotope Geochemistry, Guangzhou Institute of Geochemistry, Chinese Academy of Sciences, Guangzhou 510640, China

^b CAS Key Laboratory of Mineralogy and Metallogeny, Guangzhou Institute of Geochemistry, Chinese Academy of Sciences, Guangzhou 510640, China

^c University of Chinese Academy of Sciences, Beijing 100049, China

ARTICLE INFO

Article history:

Available online 26 September 2013

Keywords:

Layered mafic-ultramafic intrusion
Syenitic pluton
Fe-Ti oxides
Wajilitag
Tarim large igneous province

ABSTRACT

The Wajilitag igneous complex is part of the early Permian Tarim large igneous province in NW China, and is composed of a layered mafic-ultramafic intrusion and associated syenitic plutons. In order to better constrain its origin, and the conditions of associated Fe-Ti oxide mineralization, we carried out an integrated study of mineralogical, geochemical and Sr-Nd-Hf isotopic analyses on selected samples. The Wajilitag igneous rocks have an OIB-like compositional affinity, similar to the coeval mafic dykes in the Bachu region. The layered intrusion consists of olivine clinopyroxenite, coarse-grained clinopyroxenite, fine-grained clinopyroxenite and gabbro from the base upwards. Fe-Ti oxide ores are mainly hosted in fine-grained clinopyroxenite. Forsterite contents in olivines from the olivine clinopyroxenite range from 71 to 76 mol%, indicating crystallization from an evolved magma. Reconstructed composition of the parental magma of the layered intrusion is Fe-Ti-rich, similar to that of the Bachu mafic dykes. Syenite and quartz syenite plutons have $\varepsilon_{\text{Nd}}(t)$ values ranging from +1.4 to +2.9, identical to that for the layered intrusion. They may have formed by differentiation of underplated magmas at depth and subsequent fractional crystallization. Magnetites enclosed in olivines and clinopyroxenes have Cr₂O₃ contents higher than those interstitial to silicates in the layered intrusion. This suggests that the Cr-rich magnetite is an early crystallized phase, whereas interstitial magnetite may have accumulated from evolved Fe-Ti-rich melts that percolated through a crystal mush. Low V content in Cr-poor magnetite (<6600 ppm) is consistent with an estimate of oxygen fugacity of FMQ + 1.1 to FMQ + 3.5. We propose that accumulation of Fe-Ti oxides during the late stage of magmatic differentiation may have followed crystallization of Fe-Ti-melt under high $f\text{O}_2$ and a volatile-rich condition.

© 2013 Elsevier Ltd. All rights reserved.

1. Introduction

Large igneous provinces (LIPs) are sites of spatially contiguous, rapidly emplaced magmatic rocks (mostly flood basalts), which represent regions of heat and mass transfer from the mantle to the crust (Bryan and Ernst, 2008). Mafic-ultramafic intrusions and coeval felsic plutons are usually sporadically distributed in LIPs, and some of them contain economic mineralization (Schissel and Smail, 2001), such as the Noril'sk-Talnakh Ni-Cu-(PGE) sulfide deposit in the Siberian Traps (Naldrett, 2004 and references therein), Duluth Complex that hosts both Ni-Cu sulfides and Ti-Fe-V oxides in Mid-continent Rift system (Nicholson et al., 1992), the Insizwa Complex that host Ni-Cu-(PGE) sulfide mineralization in the Karoo igneous province (Lightfoot et al., 1994) and the

Skaergaard layered intrusion that hosts PGE and Au mineralization in the East Greenland Tertiary Province (Bernstein et al., 1996).

Two Permian large igneous provinces in China, the Emeishan LIP in SW China and the Tarim LIP in NW China, are both composed of voluminous flood basalts and numerous, coeval mafic-ultramafic intrusions. They are characterized by the presence of both Ni-Cu-(PGE) sulfide deposits and Fe-Ti-V oxide deposits in mafic-ultramafic intrusions (Jiang et al., 2004b, 2006; Li et al., 2008; Zhang et al., 2008, 2010a; Zhou et al., 2008, 2009; Pirajno et al., 2009). Despite numerous studies carried on the layered mafic-ultramafic intrusions hosting Fe-Ti oxide deposits, the mechanisms by which Fe, Ti and V become concentrated to form massive Fe-Ti-V oxide deposits remain enigmatic. Current metallogenetic models include fractional crystallization, magma mixing, silicate liquid immiscibility, separate magma systems, and periodic changes in oxygen fugacity ($f\text{O}_2$) (Reynolds, 1985; von Gruenewaldt et al., 1985; Harney and von Gruenewaldt, 1995; Higgins, 2005; Veksler et al., 2007; VanTongeren and Mathez, 2012). In general, the

* Corresponding author. Tel.: +86 20 8529 0109; fax: +86 20 85290261.
E-mail address: yigangxu@gig.ac.cn (Y.-G. Xu).

layered ultramafic–mafic intrusions are spatially and temporally associated with A-type granitic plutons. This link has been interpreted as evidence for silicate liquid immiscibility, fractional crystallization, crustal melting and separate magma suites (Huppert and Sparks, 1988; Ferreira et al., 1994; Weibe, 1996; Zhou et al., 2005; Veksler et al., 2007; Namur et al., 2011).

A number of mafic–ultramafic intrusions of the Tarim LIP that host economic sulfide mineralization occur in the north of the Tarim Block and the Central Asian Orogenic Belt (Pirajno et al., 2009; Zhang et al., 2010b; Qin et al., 2011; Gao et al., 2012). Association of Fe–Ti oxide-bearing layered mafic–ultramafic intrusions such as Wajilitag, Piqiang and Mazaertag with syenitic plutons in the Bachu and Atushi area, western part of the Tarim basin, is reminiscent of that in the Tarim LIP (Li et al., 2012a,b; Zhang et al., 2008, 2010a). It has been suggested that the Fe–Ti oxides were formed by two-stage fractionation in the Wajilitag layered intrusion (Li et al., 2012a). However, there has not been any attempt to study the ore-forming conditions and the link of layered mafic–ultramafic intrusion and syenitic plutons to the formation of Fe–Ti oxide mineralization.

In this study, we present mineral compositions, and whole-rock major, trace element compositions and Sr–Nd–Hf isotopes of the Wajilitag mafic–ultramafic intrusion. Together with published data for the syenitic plutons, we aim to address the following questions: (1) the nature of the parental magma of the layered mafic–ultramafic intrusion, by inference that of mantle source; (2) the formation mechanism of Fe–Ti oxide deposits and factors controlling the saturation of Fe–Ti oxides; and (3) the possible genetic link between layered mafic–ultramafic intrusion and syenitic plutons.

2. Geological background

2.1. Regional geology

The Tarim Block in NW China is bounded by the Tianshan orogenic belt in the north, and the Kunlun and Altay orogenic belt in the south (Fig. 1a). It consists of a Precambrian crystalline basement overlain by Phanerozoic strata from Ordovician to Neogene (Xinjiang Bureau of Geology and Mineral Resources, 1993; Jia, 1997). Magmatic events in the Tarim Block span a long period from ca. 2500 to 260 Ma, of which four major events occurred in Neoproterozoic to Cambrian (774–673 Ma), Ordovician (460–484 Ma), Permian (264–282 Ma) and Cretaceous (~100 Ma), respectively (Yang et al., 1997). Permian magmatic event related to the Tarim LIP is the largest one in terms of volume of igneous rocks in the Tarim Block.

2.2. Tarim large igneous province

Voluminous Permian volcanic rocks of the Tarim LIP crop out mainly in the western and southwestern parts of the basin (Jiang et al., 2004a,b,c; Yang et al., 2006, 2007; Zhang et al., 2008). Drill cores reveal that the volcanic rocks range from ~200 to >1000 m in thickness with an average of ~600 m (Fig. 1b) (Jiang et al., 2004b; Chen et al., 2006; Tian et al., 2010). The Tarim basalts erupted at ca. 290–285 Ma based on newly published zircon U–Pb ages for basalts and rhyolites in the Keping area and northern Tarim basin (Tian et al., 2010; Yu et al., 2011).

In the western part of the Tarim LIP, three layered mafic–ultramafic intrusions, Piqiang, Wajilitage and Mazaertage, intruded Silurian and Devonian strata and host economic Fe–Ti oxide mineralization (Zhang et al., 2010a), consistent with strong aero-magnetic anomalies in the Atushi, Bachu and Akesu regions (Rui et al., 2002). These intrusions were emplaced during 276–283 Ma (Yang et al., 2006; Zhang et al., 2010a; Huang et al., 2012).

In the Bachu region, mafic–ultramafic dykes are spatially associated with syenitic dykes in several outcrops, which intruded

Devonian strata (Jiang et al., 2004a; Zhou et al., 2009; Zhang et al., 2010a). Variably striking mafic dikes in the Wajilitage area intruded the upper Devonian sedimentary rocks and the mafic–ultramafic intrusion and syenitic plutons in this region. The dikes are commonly ~30 cm to ~2 m in width, with a few thick exceptions of over 5 m (Zhang et al., 2010a). These mafic and syenitic dikes have been dated at 285 ± 8 Ma and 277 ± 4 Ma, respectively (Yang et al., 2006; Zhang et al., 2010c), identical to the ages of the layered mafic–ultramafic intrusions described above. Based on the available geochemical and geochronological data (Table 1), these mafic–ultramafic intrusions and dykes, along with other igneous rocks in the Bachu region are thought to be the products of the Tarim mantle plume. (Yang et al., 2006, 2007; Zhang et al., 2010a,c; Li et al., 2012a,b; Wei et al., 2013).

2.3. Wajilitag igneous complex

The Wajilitag igneous complex in the Bachu region intruded Silurian and Devonian sedimentary rocks (Fig. 1c). The complex is about 5 km long, 1.5–3 km wide and 110–269 m in thickness, with contact zones dipping 20–40° toward the interior of the complex, as demonstrated by an extensive drill and exploration program conducted by local geological teams and Bayi steel company. The complex consists of a layered mafic–ultramafic intrusion and syenitic plutons. The former consists of olivine clinopyroxenite, clinopyroxenite and gabbro from base upwards. Clinopyroxenite makes up the major part of the intrusion, and can be further divided into coarse- (up to 5×8 mm) and fine-grained (mostly $\sim 0.5 \times 0.5$ mm) clinopyroxenite according to the grain size of clinopyroxene. Fe–Ti oxide rich layers mainly occur in the fine-grained clinopyroxenite, which contains 100 Mt of ore reserves with ca. 20 wt.% FeO_t, 7 wt.% TiO₂ and 0.14 wt.% V₂O₃ (Gao, 2007).

Syenitic plutons are sporadic in the Bachu region and are composed of syenite and quartz syenite (Fig. 1c). No evidence (e.g. chilled margin or textural contact) shows that syenite and quartz syenite are separate units. In cross-section, the syenitic plutons are underlain by the layered mafic–ultramafic intrusion and there is a sharp boundary between them. Compositinally, the syenites are intermediate to felsic. They are metaluminous with A/CNK ratios of 0.78–1.03 and A/NK values of 1.03–1.52, belonging to A₁-type granites (after Zhang et al., 2008). The syenitic plutons were dated at 274 ± 2 Ma by LA-ICP-MS (Zhang et al., 2008), slightly younger than the layered mafic–ultramafic intrusion (283 ± 2 Ma; Huang et al., 2012).

Recent screening of published ages in literature (Xu et al., 2013; Wei et al., 2013) reveals two major pulses of magmatism in the Tarim LIP, ~290 Ma and ~280 Ma. The first episode is represented by the Keping basalts, the second is mafic dykes, ultramafic–mafic–felsic complex and rhyolites. The Wajilitag complex is considered as an integral part of the second pulse, in terms of emplacement age and chemical compositions.

3. Petrography

3.1. Olivine clinopyroxenite

Olivine clinopyroxenite shows a poikilitic texture (Fig. 2a), and is composed of 50–60 vol.% clinopyroxene, 10–15 vol.% olivine, 10–20 vol.% plagioclase, 5–10 vol.% Fe–Ti oxides and <1 vol.% apatite. Olivine crystals are commonly subhedral and vary in size from 0.3 to 2 mm in diameter. Minor olivines are partially replaced by iddingsites. Plagioclase (An_{48–61}Ab_{38–50}Or_{1–2}) commonly occupies the angular interstices between olivine and clinopyroxene grains. Clinopyroxene is diopside (En_{39–42}Fs_{11–14}Wo_{45–48}), occurring as subhedral crystals with diameters ranging from 0.5 to 3 mm.

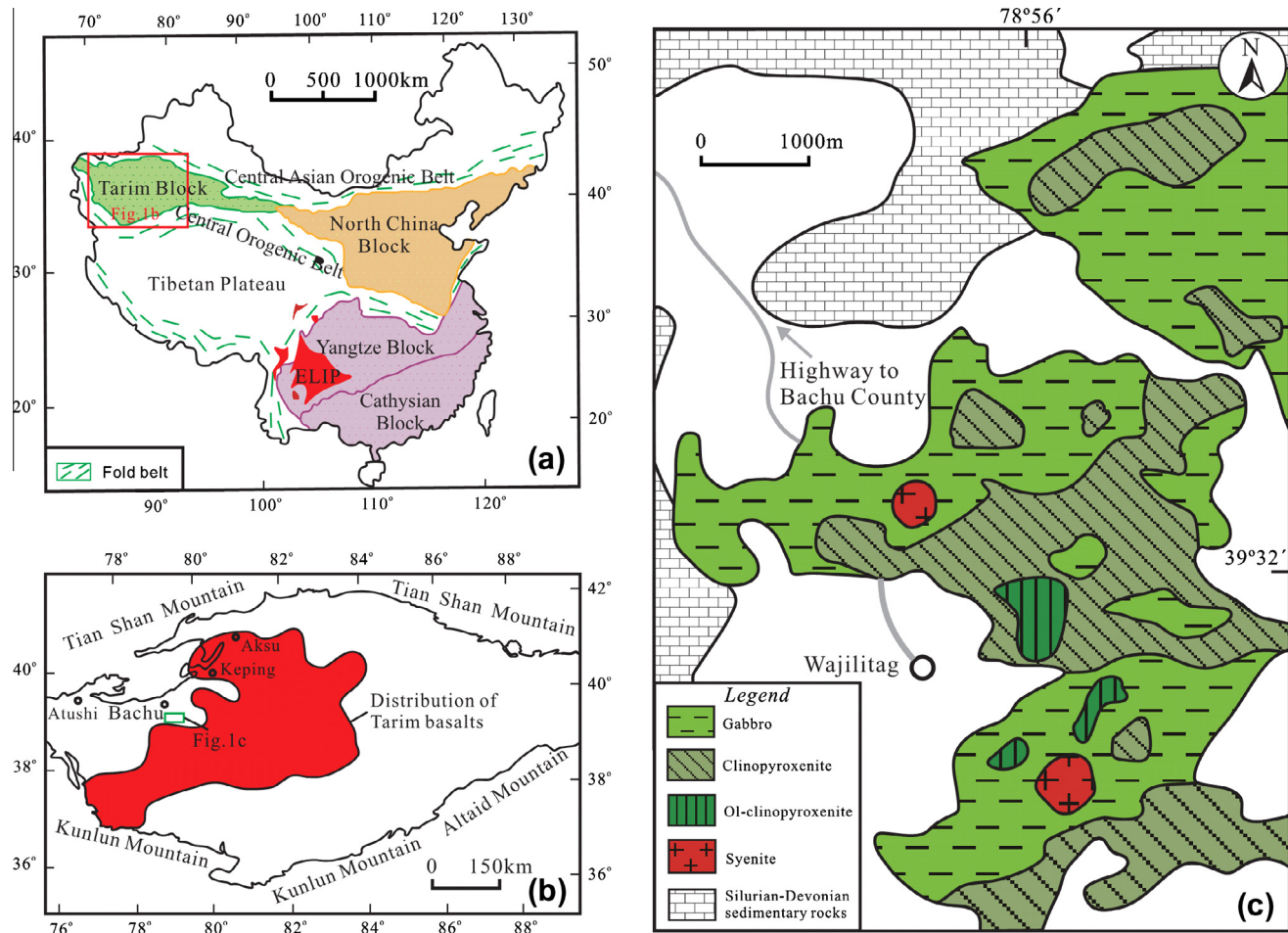


Fig. 1. Geological map of the Wajilitag complex in the west of Tarim basin (modified from Zhang et al., 2008). Inset map a showing the locations of the Tarim LIP to the northwest and Emeishan LIP to the south and map b showing the distribution of the Permian flood basalts in Tarim basin and the location of the study area (modified from Yang et al., 2005).

Table 1

Age data of the Permian igneous rocks along the northern margin of Tarim basin.

Location	Rock	Method	Age	Reference
Keping	Lower Basalt Unit	SHRIMP (Zircon)	289.5 ± 2 Ma	Yu et al. (2011)
Keping	Upper Basalt Unit	SHRIMP (Zircon)	288 ± 2 Ma	Yu et al. (2011)
Northern Tarim basin	Rhyolite	SHRIMP (Zircon)	277.3 ± 2.5 Ma	Tian et al. (2010)
Northern Tarim basin	Rhyolite	LA-ICP-MS (Zircon)	290.9 ± 4.1 Ma	Tian et al. (2010)
Northern Tarim basin	Rhyolite	LA-ICP-MS (Zircon)	286.6 ± 3.3 Ma	Tian et al. (2010)
Northern Tarim basin	Rhyolite	LA-ICP-MS (Zircon)	282.9 ± 2.5 Ma	Tian et al. (2010)
Northern Tarim basin	Rhyolite	LA-ICP-MS (Zircon)	271.7 ± 2.2 Ma	Tian et al. (2010)
Bachu	Mafic dyke	Ar-Ar (Whole rock)	285.4 ± 8.5 Ma	Zhang et al. (2010c)
Mazaertage	Syenitic dyke	SHRIMP (Zircon)	277 ± 4 Ma	Yang et al. (2006)
Mazaertage	Syenite	Ar-Ar (Whole rock)	277 ± 1.3 Ma	Yang et al. (1996)
Mazaertage	Syenite	Cameca (Zircon)	279.7 ± 2 Ma	Wei and Xu (2011)
Wajilitag	Gabbro	Cameca (Zircon)	283 ± 2 Ma	Huang et al. (2012)
Wajilitag	Quartz syenite	LA-ICP-MS (Zircon)	273.7 ± 1.5 Ma	Zhang et al. (2008)

Fe-Ti oxides mainly consist of magnetite (90–95%) and minor ilmenite. Magnetites occur either as inclusions in olivine and clinopyroxene or as interstitial to silicate minerals (Fig. 2a and b). Small irregular ilmenite grains occur in the margins of magnetites or as lamellae in interstitial magnetites.

3.2. Coarse-grained clinopyroxenite

Coarse-grained clinopyroxenite contains 75–80 vol.% clinopyroxene and 5–10 vol.% Fe-Ti oxides and <3 vol.% olivine. Subhedral and anhedral clinopyroxene grains range in size from 0.5×0.5 mm

to 8×5 mm and contain two sets of exsolution lamellae marked by Fe-Ti oxide laths parallel to prismatic cleavage planes. The clinopyroxene is diopside ($\text{En}_{39-43}\text{Fs}_{10-15}\text{Wo}_{45-48}$). Most Fe-Ti oxides are interstitial to silicate minerals (Fig. 2c). Euhedral and subehedral magnetite inclusions in clinopyroxene are commonly surrounded by irregular ilmenite grains.

3.3. Fine-grained clinopyroxenite

Fine-grained clinopyroxenite consists of 70–85 vol.% clinopyroxene and 15–20 vol.% Fe-Ti oxides. Clinopyroxene

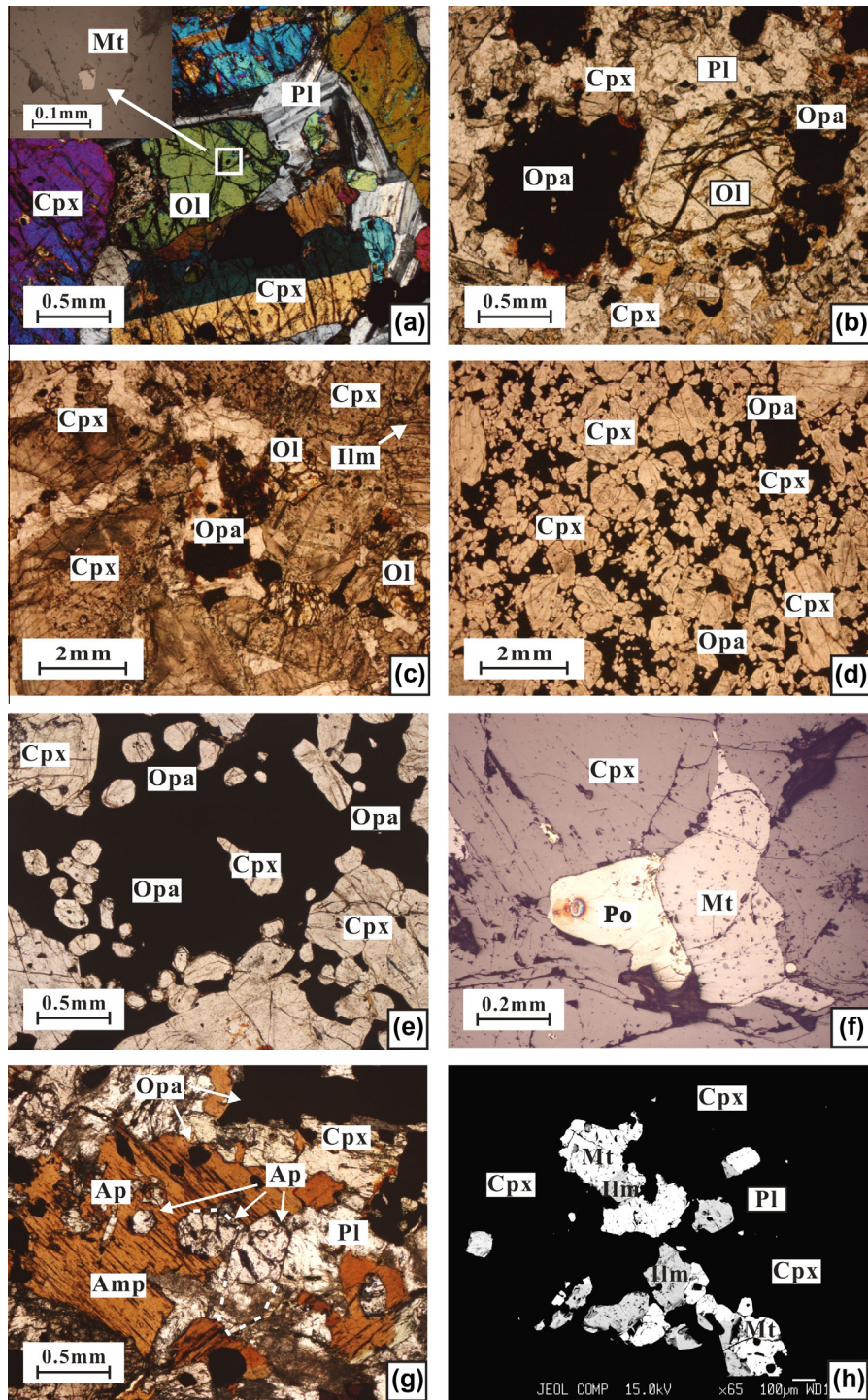


Fig. 2. Microphotographs of samples from the Wajilitag mafic-ultramafic intrusion, NW China. (a) A poikilitic texture of olivine (Ol) cumulates are enclosed in clinopyroxene (Cpx) and plagioclase (Pl). Minor fine-grained euhedral magnetite (Mt) is enclosed in olivine. Needle-like apatite is also present. Under cross-polarizer, transmitted light, sample BC1174; (b) Interstitial Fe-Ti oxides in olivine clinopyroxenite. Under plane-polarizer, transmitted light, sample BC1174; (c) Net-texture of unequigranular clinopyroxene filled with interstitial Fe-Ti oxides in coarse-grained clinopyroxenite. Minor fine-grained euhedral magnetite and ilmenite is enclosed in clinopyroxene. note the presence of ilmenite lamellae along prismatic cleavages of the clinopyroxene host. Under plane-polarizer, transmitted light, sample BC1118; (d) Net-texture of equigranular clinopyroxene filled with interstitial Fe-Ti oxides in fine-grained clinopyroxenite. Under plane-polarizer, transmitted light, sample BC1149; (e) Cumulus oxide ores with equigranular clinopyroxene. Under plane-polarizer, transmitted light, sample BC1128; (f) Equilibrium texture of pyrrhotite along the boundaries of magnetite in the Fe-Ti oxide ore. Under reflected light, sample BC1128; (g) an ophitic texture of gabbro showing cumulus clinopyroxene, plagioclase, Fe-Ti oxides and apatite in gabbro with interlocking boundaries. Under plane-polarizer, transmitted light, sample BC1107; (h) Coexisting magnetite and ilmenite, as well as oriented ilmenite exsolution lamellae in the magnetite (BC1107). BSE images of Fe-Ti oxide minerals in Gabbro.

(En_{39–43}Fs_{11–13}Wo_{46–50}) commonly has a granular morphology and most grains are about 0.5 × 0.5 mm in size (Fig. 2d). Fe-Ti oxides interstitial to silicate minerals consist of magnetite (50–70%) and

ilmenite (30–50%). Euhedral and subhedral ilmenite grains are commonly intergrown with magnetite or as oriented exsolution lamellae in magnetite.

3.4. Oxide clinopyroxenite

Clinopyroxenite with >25% Fe_2O_3 (total) is referred as oxide clinopyroxenite in this study, following the classification scheme for the Panzhihua intrusion in the Emeishan LIP (Pang et al., 2009). Most oxide clinopyroxenite show net texture with Fe–Ti oxides interstitial to clinopyroxene (Fig. 2e). Minor sulfides (pyrrhotite + chalcopyrite ± pentlandite) also occur in the interstitial phase in fine-grained clinopyroxenite (Fig. 2f).

3.5. Gabbro

Gabbro has an ophitic texture and is composed of 40–50 vol.% plagioclase and 35–45 vol.% clinopyroxene, <10 vol.% Fe–Ti oxides, <5 vol.% hornblende and <5 vol.% apatite. Plagioclase laths range from 0.2 to 1 mm in width and are andesine ($\text{An}_{42-46}\text{Ab}_{52-57}\text{Or}_{1-2}$). Clinopyroxene ($\text{En}_{39-43}\text{Fs}_{10-15}\text{Wo}_{45-48}$) is commonly rimmed by hornblende. Euhedral apatite crystals range from 0.075×0.05 mm to 0.75×0.3 mm in size, whereas there are also some needle-like apatite crystals which are almost visible (Fig. 2g). Fe–Ti oxides interstitial to silicate minerals consist of magnetite (40–60%) and ilmenite (40–60%). Magnetite grains commonly have ilmenite lamellae as trellis and tiny lenses parallel to the {111} planes. Small irregular ilmenite grains also occur in the margins of magnetite (Fig. 2h).

3.6. Syenite and quartz syenite

According to Li et al. (2001) and Zhang et al. (2008), syenite has intermediate- to fine-grained texture and consists dominantly of orthoclase (40–60 vol.%), aegirine-augite (40–50 vol.%) and subordinate nepheline (0–5 vol.%) and biotite (1–5 vol.%). Small amounts of apatite and allanite are also present. Quartz syenite has similar texture to syenite and is mainly composed of orthoclase (40–70 vol.%), quartz (10–30 vol.%), hornblende (5–10 vol.%) and minor biotite (1–2 vol.%). There is a small amount of zircon, apatite, rutile, allanite and monazite.

4. Analytical methods

Representative samples were collected from a section in the open pit. Relatively fresh samples were selected and sawed into slabs and the central parts were used for preparing thin sections and whole-rock chemical analyses. Eleven thin sections and 48 whole-rock samples were analyzed for minerals and whole-rock compositions. All the analyses were carried out at the State Key Laboratory of Isotope Geochemistry, Guangzhou Institute of Geochemistry, Chinese Academy of Sciences (GIGCAS).

4.1. Whole-rock major elements

Major element oxides were determined on fusion glasses with a ratio of 1:8 for sample to $\text{Li}_2\text{B}_4\text{O}_7$ flux, using a Rigaku ZX100e X-ray fluorescence spectrometer. The accuracies of the XRF analyses are estimated to be better than 1% for SiO_2 , better than 2% for other major oxides present in concentrations greater than 0.5 wt.% and 5 wt.% for MnO and P_2O_5 . Detailed analytical procedures can be found in Li et al. (2006).

Trace elements, including rare earth element (REE), were analyzed by a Perkin–Elmer ELAN 6000 inductively-coupled plasma source mass spectrometer (ICP-MS) following procedures described by Li et al. (2002). ~50 mg sample powders were dissolved in screw-top Teflon beakers using an $\text{HF} + \text{HNO}_3$ mixture for 7 days at $\sim 100^\circ\text{C}$. An internal standard solution containing the single element Rh was used to monitor drift in mass response during counting. Three USGS standards G-2, W-2 and BCR-1 and two Chinese

standards GSR-1 and GSR-3 were used to calibrate the elemental concentrations of the measured samples. Analytical precision for most elements was better than 5%.

4.2. Rb–Sr, Sm–Nd and Lu–Hf isotopes

Sr–Nd–Hf isotope ratios and concentrations of Rb, Sr, Nd and Hf were determined using a Finnigan Neptune multicollector (MC)-ICP-MS, following the procedure described by Li et al. (2005). Measured $^{87}\text{Sr}/^{86}\text{Sr}$, $^{143}\text{Nd}/^{144}\text{Nd}$ and $^{176}\text{Hf}/^{177}\text{Hf}$ ratios were normalized to $^{86}\text{Sr}/^{88}\text{Sr} = 0.1194$, $^{146}\text{Nd}/^{144}\text{Nd} = 0.7219$ and $^{179}\text{Hf}/^{177}\text{Hf} = 0.7325$ respectively. The reported $^{87}\text{Sr}/^{86}\text{Sr}$, $^{143}\text{Nd}/^{144}\text{Nd}$ and $^{176}\text{Hf}/^{177}\text{Hf}$ ratios were adjusted relative to NBS SRM 987 standard $^{87}\text{Sr}/^{86}\text{Sr} = 0.71025$, Shin Etsu JNd-1 standard $^{143}\text{Nd}/^{144}\text{Nd} = 0.512115$, and JB-3 standard $^{176}\text{Hf}/^{177}\text{Hf} = 0.282160$, respectively.

4.3. Mineral compositions

Major element compositions of minerals were determined with a JEOL JXA-8100 electron microprobe at GIGCAS, using a beam of 15 keV and 20 nA focused to a spot of $\sim 2 \mu\text{m}$ in diameter. Peak and background counting times were set at 30 and 15 s, respectively. The standards used for oxide analyses were spinel for Mg and Al, diopside for Si, ilmenite for Ti, vanadium metal for V, chromite for Cr and Fe, manganese oxide for Mn, niccolite (NiAs) for Ni, cobalt metal for Co, and sphalerite for Zn. Because of overlap between Ti K β and V K α peaks (Carmichael, 1967), concentrations of V were corrected on the basis of interferences between Ti and V. Concentrations of V after correction for Ti K β peak are mostly less than 1 wt.%. Ferrous and ferric iron were estimated from stoichiometry and charge balance. The precision of the analyses is better than 5% for major elements. Representative analyses are listed in Supplementary Tables 1–7.

5. Results

5.1. Whole-rock major oxides

The analyzed samples have small loss-on-ignition (LOI = –0.9 to 1.2 wt.%; Table 2). All the rocks show alkaline affinities in terms of total alkalis versus SiO_2 (Fig. 3). Oxide clinopyroxenite and fine-grained clinopyroxenite have 10.7–11.7 wt.% MgO , 23.6–28.5 wt.% Fe_2O_3 t, and 7.2–9.7 wt.% TiO_2 , higher than other members of the intrusion. There are negative correlations between Fe_2O_3 t, TiO_2 and SiO_2 , consistent with fractionation of Fe–Ti oxides (Fig. 3).

Olivine clinopyroxenites have 41.5–44.8 wt.% SiO_2 and 7.4–14.4 wt.% MgO . From olivine clinopyroxenite to gabbro, CaO , Fe_2O_3 t and TiO_2 decrease with increasing SiO_2 , whereas Al_2O_3 and $\text{Na}_2\text{O} + \text{K}_2\text{O}$ increase (Fig. 3). These correlations indicate accumulation of clinopyroxene, plagioclase and Fe–Ti oxides. The negative correlation of P_2O_5 and SiO_2 is consistent with the presence of cumulus apatite in the rocks. These variations are consistent with inferred crystallization sequence of Ol→Cpx→Pl→Ap, as observed in thin sections.

Syenites have 56.2–64.0 wt.% SiO_2 and 8.0–11.7 wt.% total $\text{Na}_2\text{O} + \text{K}_2\text{O}$, whereas quartz syenites have 67.9–68.7 wt.% SiO_2 and 10.3–12.0 wt.% total $\text{Na}_2\text{O} + \text{K}_2\text{O}$. From syenite to quartz syenite, MgO , Fe_2O_3 t, TiO_2 , Al_2O_3 , CaO and P_2O_5 decrease, whereas total $\text{Na}_2\text{O} + \text{K}_2\text{O}$ increase with increasing SiO_2 (Fig. 3), consistent with the fractionation of clinopyroxene, plagioclase, apatite and Fe–Ti oxides.

5.2. Whole-rock trace elements

Fine-grained clinopyroxenite and oxide clinopyroxenite are rich in V (>710 ppm, Table 2). The positive correlation between V and

Table 2

Whole-rock compositions of major rock types in the Wajilitag complex

Sample no.	BC1101	BC1102	BC1103	BC1104	BC1105	BC1106	BC1107	BC1108	BC1109	BC1110	BC1111	BC1112	BC1114A	BC1114B
Rock type	GB	GB												
SiO ₂ (wt.%)	46.04	44.37	43.27	43.87	50.01	46.02	49.53	47.94	45.87	51.23	50.58	50.01	50.55	45.76
TiO ₂	4.15	4.94	5.39	4.65	2.94	3.84	2.92	3.89	4.15	2.38	2.55	2.98	2.38	4.25
Al ₂ O ₃	15.10	12.49	10.43	11.69	18.10	14.59	18.62	13.57	12.91	18.91	18.69	18.03	19.04	12.72
Fe ₂ O ₃	12.41	16.32	16.28	16.11	9.68	14.05	10.27	14.52	15.81	8.96	9.46	9.92	8.96	16.17
MnO	0.16	0.19	0.19	0.20	0.13	0.16	0.15	0.19	0.19	0.12	0.13	0.14	0.12	0.21
MgO	5.63	6.03	7.93	7.16	3.47	5.34	3.23	4.82	5.15	2.98	3.07	3.29	2.94	5.24
CaO	10.12	10.69	11.28	11.18	8.58	10.20	7.55	7.83	9.24	6.90	7.18	8.06	7.34	8.56
Na ₂ O	3.18	2.46	2.06	2.35	3.96	3.00	4.41	3.25	2.76	4.37	4.28	4.33	4.29	2.80
K ₂ O	1.58	1.32	1.72	1.38	1.65	1.41	1.57	2.35	2.00	2.21	2.15	1.54	2.16	2.01
P ₂ O ₅	0.89	0.76	0.61	0.62	0.44	0.85	0.51	0.71	0.82	0.54	0.63	0.65	0.54	0.91
LOI	0.27	-0.03	0.38	0.32	0.57	0.05	0.77	0.45	0.64	0.93	0.80	0.57	1.22	0.90
Total	99.52	99.52	99.52	99.52	99.53	99.52	99.53	99.52	99.53	99.53	99.53	99.52	99.54	99.53
Mg-no.	50.0	44.9	51.7	49.5	44.1	45.6	40.9	42.2	41.8	42.3	41.7	42.2	41.9	41.6
Sc (ppm)	17.39	26.92	30.44	25.98	13.07	20.03	9.61	17.7	18.77	8.91	8	11.12	6.74	20.37
V	299.1	393.1	431.4	345.4	186.3	314.3	175.3	313.6	337.1	138.8	158.1	181	145.7	347.9
Cr	16.99	20.82	137.1	153.3	14.07	15.45	8.35	4.38	3.73	3.28	5.67	0.75	1.26	2.89
Co	41.25	53.6	55.08	54.01	26.55	42.96	31.57	40.66	45.51	24.46	25.74	25.83	24.08	48.42
Ni	47.64	53.35	99.86	98.98	27.88	34.53	29.12	17.8	11.83	16.42	16.75	12.96	16.96	15.75
Cu	63.91	106.2	55.15	112.1	36.14	51.95	75.2	47.55	80.55	24.57	26.21	24.6	26.52	118.9
Rb	34.59	32.04	51.32	33.93	34.25	30.77	39.89	51.11	48.14	42.67	41.81	32	43.99	48.5
Sr	1130.8	873.8	583.3	743.7	1276	1100.8	1225.7	972.3	874.9	1124	1161	1349.8	1130.1	868.4
Y	26.96	27.46	31.37	25.37	22.32	31.35	19.54	31.21	33.35	22.32	22.44	22.49	20.08	37.48
Zr	285.7	258	359.2	267.4	330.9	262.2	261.9	305	321	299.5	318.1	257.1	232.9	298.3
Nb	46.87	54.68	67.55	44.02	50.61	49.86	49.72	61.18	57.54	45.04	46.2	47.5	41.74	57.16
Ba	692.2	501.6	581.8	606.5	1147.4	737.8	1048.6	771.1	773.5	996.9	906.3	752.6	1001.4	993.5
La	60.41	46.25	46.37	39.29	53.53	69.54	53.62	59.8	66.77	52.08	53.01	48.6	49.26	70.7
Ce	126.5	99.23	102.8	87.53	106.9	139.9	106.2	129.2	142.6	106	105.4	99.2	99.02	149.9
Pr	16.05	13.74	14.59	12.21	12.83	17.82	12.63	16.57	18.54	13.15	13.28	12.82	12.42	20.32
Nd	64.04	57.65	63.03	51.4	49.79	71.47	49.29	66.37	73.95	51.35	53.7	52.14	47.98	82.06
Sm	12.2	11.49	12.9	10.61	9.22	13.96	9.02	12.82	14.46	9.68	9.81	9.99	8.99	16.33
Eu	3.66	3.5	3.25	3.26	3.96	4.13	3.89	3.78	4.08	4.03	3.98	4.04	3.99	4.52
Gd	10.19	10.04	11.18	9.42	8	12.13	7.46	10.9	12.42	8.12	8.4	8.69	7.66	13.82
Tb	1.39	1.36	1.55	1.26	1.07	1.57	0.97	1.5	1.64	1.07	1.11	1.13	1	1.86
Dy	6.75	6.91	8.08	6.38	5.27	7.91	4.99	7.43	8.1	5.47	5.58	5.49	4.89	9.2
Ho	1.17	1.24	1.43	1.12	0.98	1.4	0.87	1.35	1.47	0.96	0.99	0.98	0.87	1.61
Er	2.65	2.81	3.29	2.55	2.26	3.27	2	3.05	3.33	2.23	2.25	2.21	1.97	3.76
Tm	0.34	0.36	0.43	0.33	0.29	0.42	0.27	0.4	0.43	0.3	0.29	0.28	0.26	0.47
Yb	2	2.16	2.57	1.95	1.82	2.35	1.55	2.31	2.57	1.82	1.8	1.66	1.55	2.71
Lu	0.28	0.31	0.37	0.27	0.27	0.33	0.23	0.34	0.37	0.26	0.26	0.24	0.22	0.38
Hf	6.89	6.69	9.71	7.2	8.07	6.7	6.51	7.77	8.69	7.71	7.86	6.18	5.47	7.67
Ta	3.33	3.71	4.81	2.99	3.25	3.35	3.35	4.18	3.99	3.05	2.97	3.13	2.82	3.71
Th	5.25	5.17	5.57	4.32	6.19	4.54	5.9	5.29	7.71	8.05	5.94	5.65	7.19	5.77
U	1.27	1.29	1.37	1.25	1.51	1.13	1.44	1.3	1.68	1.76	1.38	1.34	1.36	1.27
(La/Yb) _N	21.67	15.35	12.95	14.45	21.14	21.25	24.85	18.61	18.64	20.57	21.15	20.95	22.75	18.71
(Gd/Yb) _N	4.21	3.84	3.60	4.00	3.65	4.28	3.99	3.91	4.00	3.70	3.86	4.32	4.08	4.22
Eu/Eu*	1.00	1.00	0.83	1.00	1.41	0.97	1.45	0.98	0.93	1.39	1.34	1.33	1.47	0.92
	BC1115	BC1116	BC1117	BC1118	BC1119	BC1123	BC1124	BC1125	BC1126	BC1127	BC1128	BC1129	BC1130	BC1131
	CCP	CCP	CCP	CCP	OCP	OCP								
SiO ₂ (wt.%)	44.00	45.88	44.63	45.77	46.29	33.00	33.00	33.82	34.50	34.55	33.44	33.61	33.96	34.68
TiO ₂	3.25	3.62	3.69	3.81	3.59	8.61	8.58	8.32	7.70	7.86	8.33	8.33	8.15	7.59
Al ₂ O ₃	5.72	7.63	7.72	7.85	7.68	3.94	3.86	3.80	3.95	4.05	3.99	3.99	3.92	4.09
Fe ₂ O ₃	17.69	13.75	16.50	13.81	14.01	28.48	27.94	26.70	25.74	26.06	27.76	27.67	27.17	25.78
MnO	0.20	0.18	0.19	0.17	0.18	0.20	0.21	0.22	0.19	0.20	0.20	0.20	0.20	0.20
MgO	14.27	12.39	12.10	12.16	12.26	10.97	11.24	10.69	11.40	11.28	11.02	11.09	11.03	11.49
CaO	13.00	14.64	12.14	14.34	14.06	14.88	15.10	14.96	15.95	15.45	15.24	15.25	15.31	15.70
Na ₂ O	0.99	1.15	1.38	1.23	1.17	0.25	0.32	0.25	0.33	0.30	0.29	0.27	0.29	0.36
K ₂ O	0.57	0.42	0.96	0.47	0.43	0.01	0.03	0.01	0.04	0.04	0.02	0.02	0.02	0.06
P ₂ O ₅	0.13	0.11	0.28	0.12	0.11	0.01	0.01	0.00	0.01	0.01	0.01	0.01	0.01	0.02
LOI	-0.30	-0.24	-0.08	-0.22	-0.25	-0.83	-0.76	0.69	-0.31	-0.28	-0.78	-0.90	-0.56	-0.43
Total	99.52	99.52	99.52	99.52	99.52	99.52	99.52	99.47	99.52	99.52	99.53	99.53	99.53	99.52
Mg-no.	64.0	66.5	61.7	66.0	65.8	45.9	47.0	46.8	49.4	48.8	46.6	46.9	47.2	49.5
Sc (ppm)	48.16	53.37	42.24	52.73	47.74	59.68	58.24	63.63	61.91	58.51	64.43	59.07	59.93	60.23
V	447.4	388.2	400.9	385	376.2	829.3	865.2	823.6	822.2	786.4	958.1	823.6	855.5	788.8
Cr	518.3	710.5	413.5	638	632.2	281.6	280.8	288.4	344.5	308.4	296.6	270.7	270.6	238.6
Co	86.47	67.15	76.6	70.96	68.05	121.3	119.5	122.9	111.3	109.2	133.5	115.3	113	109
Ni	290.5	213.6	239	221.2	219	226.5	213.7	235	214.5	193.6	237.7	199.6	197.1	205.9
Cu	45.98	53.53	36.71	53.05	49.82	241.6	202.7	247.1	169.3	174.2	278.4	208.9	214.6	183.1
Rb	15.96	11.45	22.89	12.68	11.15	0.24	0.37	0.29	0.37	1.08	0.3	0.28	0.39	0.82
Sr	283.4	412.8	424.2	437.9	410.9	75.73	79.27	80.79	83.02	81.08	90.25	76.8	85.88	87.58
Y	16.73	15.35	19.99	15.49	14.42	13.47	13.51	14.31	13.81	13.85	15.23	13.33	14.06	14.16
Zr	176.4	151	235	164.4	152.5	93.55	89	94.3	91.09	92.94	105.1	90.88	90.77	94.46

Table 2 (continued)

	BC1115 CCP	BC1116 CCP	BC1117 CCP	BC1118 CCP	BC1119 CCP	BC1123 OCP	BC1124 OCP	BC1125 OCP	BC1126 OCP	BC1127 OCP	BC1128 OCP	BC1129 OCP	BC1130 OCP	BC1131 OCP
Nb	19.8	18.6	31.4	20.35	18.28	9.66	12.6	6.55	10.11	10.59	12.79	11.53	11.81	10.18
Ba	238	185.6	341.9	212.1	206.3	7.53	12.98	10.31	5.89	19.75	7.34	5.68	15.7	13.4
La	17.79	13.93	27.47	14.99	14.05	3.92	3.79	4.16	4.03	4.37	4.31	3.98	3.97	4.24
Ce	42.69	33.88	60.87	36.13	33.19	14.73	14.32	15.5	14.61	15.55	15.2	14.65	14.08	15.28
Pr	6.33	5	8.45	5.31	4.95	2.9	2.84	3.07	2.91	3.03	3.18	2.85	2.84	2.91
Nd	28.04	22.87	36.19	24.16	22.5	16.39	15.84	16.95	16.11	16.51	17.17	15.83	16.15	15.94
Sm	6.5	5.66	7.51	5.83	5.47	4.89	4.7	5	4.68	4.83	5.25	4.76	4.83	4.7
Eu	1.97	1.8	2.22	1.85	1.72	1.46	1.45	1.53	1.43	1.48	1.59	1.44	1.49	1.45
Gd	5.91	5.33	6.9	5.51	5.06	4.86	4.76	5.03	4.72	5	5.19	4.72	4.7	4.72
Tb	0.83	0.74	0.95	0.76	0.71	0.72	0.68	0.75	0.69	0.71	0.75	0.7	0.69	0.67
Dy	4.26	3.88	4.83	3.99	3.71	3.75	3.6	3.88	3.6	3.69	3.98	3.73	3.63	3.67
Ho	0.78	0.68	0.85	0.7	0.66	0.65	0.63	0.68	0.64	0.65	0.69	0.64	0.65	0.63
Er	1.74	1.55	1.94	1.58	1.45	1.44	1.41	1.48	1.36	1.45	1.55	1.4	1.43	1.41
Tm	0.22	0.19	0.25	0.2	0.19	0.18	0.17	0.18	0.17	0.18	0.18	0.17	0.17	0.17
Yb	1.3	1.16	1.46	1.17	1.12	1.03	0.97	1.02	0.96	1.03	1.07	0.97	0.95	0.97
Lu	0.19	0.16	0.22	0.18	0.16	0.14	0.14	0.15	0.14	0.14	0.15	0.14	0.14	0.14
Hf	5.01	4.31	5.85	4.61	4.35	3.36	3.42	3.38	3.29	3.45	3.75	3.35	3.32	3.23
Ta	1.43	1.41	2.16	1.53	1.4	0.84	1.07	0.45	0.95	1.07	1.2	1.1	1.12	0.95
Th	2.09	1.69	3.33	1.97	1.93	0.06	0.07	0.07	0.1	0.14	0.09	0.08	0.09	0.27
U	0.64	0.45	0.84	0.51	0.55	0.02	0.03	0.02	0.03	0.03	0.03	0.02	0.02	0.05
(La/Yb) _N	9.82	8.59	13.50	9.16	8.97	2.73	2.80	2.93	3.00	3.05	2.90	2.94	3.00	3.14
(Gd/Yb) _N	3.76	3.79	3.91	3.89	3.73	3.91	4.06	4.09	4.06	4.03	4.02	4.01	4.10	4.03
Eu/Eu*	0.97	1.00	0.94	0.99	1.00	0.92	0.93	0.93	0.92	0.93	0.93	0.96	0.94	
	BC1138 OCP	BC1139 OCP	BC1140 OCP	BC1142 OCP	BC1146 OCP	BC1149 OCP	BC1137A FCP	BC1137B FCP	BC1141 FCP	BC1147 FCP	BC1148 FCP	BC1171 OI-CP	BC1172 OI-CP	BC1173 OI-CP
SiO ₂ (wt.%)	34.72	33.85	34.89	32.68	33.30	35.50	36.11	35.89	36.36	36.50	36.67	42.67	44.82	41.76
TiO ₂	7.81	7.25	7.75	9.70	8.65	7.64	7.60	7.35	7.25	7.79	7.21	3.68	4.04	4.98
Al ₂ O ₃	3.92	3.92	3.93	3.51	4.04	4.07	3.78	3.92	4.44	3.90	3.93	7.08	12.41	8.16
Fe ₂ O ₃	25.85	25.78	25.86	28.25	26.80	25.25	24.51	24.49	24.29	23.63	24.38	17.12	15.16	17.61
MnO	0.20	0.20	0.20	0.17	0.18	0.20	0.21	0.20	0.22	0.19	0.18	0.2	0.19	0.17
MgO	11.71	11.40	11.59	10.71	10.97	10.94	11.10	11.49	10.92	10.99	11.07	14.1	7.44	11.08
CaO	15.61	16.08	15.68	14.81	15.23	15.57	15.75	15.90	15.39	15.91	15.71	12.84	10.59	14.02
Na ₂ O	0.27	0.30	0.27	0.27	0.31	0.30	0.28	0.30	0.48	0.30	0.32	1.24	2.76	1.29
K ₂ O	0.02	0.03	0.01	0.03	0.07	0.02	0.01	0.03	0.12	0.03	0.04	0.5	1.28	0.34
P ₂ O ₅	0.01	0.01	0.01	0.01	0.01	0.01	0.01	0.01	0.04	0.01	0.01	0.48	0.84	0.2
LOI	-0.60	0.72	-0.66	-0.62	-0.04	0.01	0.08	-0.06	0.00	0.26	-0.01	-0.4	0.01	-0.1
Total	99.52	99.53	99.52	99.52	99.52	99.52	99.45	99.52	99.52	99.52	99.52	99.52	99.52	99.52
Mg-no.	49.9	49.3	49.7	45.5	47.4	48.8	49.9	50.8	49.8	50.6	50.0	64.5	51.9	58.1
Sc (ppm)	60.06	57.7	63.21	68.25	56.88	63.17	58.92	60.07	60.78	63.61	59.37	37.89	25.44	55.16
V	763.8	796	801.7	855	814.5	800.3	751.8	763.5	751.1	753.9	796.1	384.8	332.1	754.3
Cr	289.5	368.3	329.1	12.15	4.86	282.2	354.4	303.7	299.5	320.9	217.2	623.8	186.5	184.1
Co	109.9	112	113.4	109.1	101.1	95.24	104.4	106.1	103.7	85.31	86.56	86.15	54.88	83.37
Ni	202	231.4	214.9	210.1	204.5	179.9	185.3	188.9	192.5	146.2	217.5	380.1	129.1	215.9
Cu	192.9	418.6	150.1	197.9	233.9	284.3	220	214.7	214.4	368.4	71.63	91.21	38.7	63.58
Rb	0.45	0.57	0.24	1.27	4.72	0.43	0.52	0.55	2.18	0.44	7.13	12.27	29.39	7.69
Sr	86.31	117.4	86.7	72.4	75.23	90.61	99.14	119.1	163.7	89.37	581.3	695.5	1180.7	614.2
Y	13.59	14.51	14.2	10.43	11.95	16.48	13.56	14.17	17.59	16.31	17.96	20.81	30.46	17.56
Zr	91.33	86.84	92.81	82.2	93.94	101.6	89.43	91.77	108	109.6	163.4	193.1	279.2	169.4
Nb	10.62	9.6	10.89	4.07	9.51	11.54	10.66	13.25	37.96	10.31	24.56	56.81	25.4	
Ba	56.79	132.1	127.54	59.48	81.44	170.0	182.2	149.6	486.6	108.28	166.5	308.3	546.2	178.7
La	4.08	4.02	3.94	3.03	3.94	4.71	4.03	3.95	8.51	4.96	19.22	34.78	59.41	20.12
Ce	14.5	14.39	14.77	10.75	13.28	17.58	14.98	14.03	33.08	18.24	45.44	78.4	126.6	46.4
Pr	2.89	2.89	2.92	2.11	2.5	3.43	2.9	2.88	6.79	3.56	6.6	10.55	17.36	6.91
Nd	16.01	16.16	16.17	11.71	13.76	18.91	16.16	16.01	36.24	19.5	30.52	44.56	72.88	31.43
Sm	4.81	4.82	4.81	3.6	4.18	5.68	4.79	4.71	10.07	5.61	7.16	9.09	14.09	7.21
Eu	1.41	1.5	1.46	1.12	1.29	1.71	1.55	1.7	2.83	1.68	2.19	2.71	4.2	2.19
Gd	4.75	4.85	4.81	3.59	4.25	5.51	4.79	4.84	8.27	5.64	6.58	8.15	12.15	6.46
Tb	0.7	0.7	0.72	0.52	0.61	0.82	0.67	0.69	1.03	0.83	0.91	1.08	1.56	0.88
Dy	3.62	3.73	3.77	2.74	3.13	4.33	3.63	3.6	4.92	4.25	4.5	5.35	7.64	4.41
Ho	0.64	0.66	0.66	0.47	0.55	0.75	0.63	0.64	0.79	0.76	0.78	0.94	1.36	0.79
Er	1.39	1.44	1.45	1.05	1.22	1.69	1.39	1.39	1.7	1.62	1.76	2	2.98	1.72
Tm	0.17	0.18	0.17	0.12	0.15	0.2	0.17	0.17	0.2	0.2	0.21	0.25	0.37	0.21
Yb	1	1.02	1.02	0.72	0.88	1.15	0.95	0.99	1.18	1.2	1.26	1.47	2.2	1.29
Lu	0.14	0.14	0.14	0.1	0.12	0.16	0.14	0.14	0.17	0.17	0.18	0.21	0.31	0.17
Hf	3.37	3.11	3.32	2.87	3.54	3.62	3.28	3.23	3.63	3.88	4.79	5.12	7.32	4.69
Ta	0.92	0.85	1.03	0.23	0.79	1.08	1.01	0.99	1.2	0.81	1.81	1.8	4.18	1.84
Th	0.11	0.27	0.07	0.08	0.36	0.07	0.1	0.19	0.3	0.1	0.4	2.19	4.37	1.51
U	0.02	0.02	0.02	0.07	1.31	0.02	0.02	0.02	0.07	0.05	0.37	0.57	1.15	0.39
(La/Yb) _N	2.93	2.84	2.77	3.01	3.21	2.94	3.04	2.85	5.16	2.96	4.10	17.03	19.34	11.17
(Gd/Yb) _N	3.94	3.95	3.90	4.11	3.99	3.97	4.15	4.03	5.78	3.89	4.31	4.6	4.56	4.14
Eu/Eu*	0.90	0.95	0.93	0.95	0.93	0.94	0.99	1.09	0.95	0.91	0.98	0.96	0.98	0.98

(continued on next page)

Table 2 (continued)

	BC1174 OI-CP	BC1175 OI-CP	05BH-1 S	05BH-4 S	05BH-6 S	05BH-7 S	05BH-8 S	05BH-9 S	05BH-10 S	05BH-11 S	Wp-63 S	05BH-2 QS	05BH-3 QS	05BH-5 QS	W13 DB
SiO ₂ (wt.%)	42.51	41.46	61.42	63.97	60.62	62.29	62.24	59.85	56.23	56.46	58.3	68.7	68.48	67.87	46.74
TiO ₂	3.72	5.16	0.54	0.42	0.75	0.56	0.6	0.88	1.46	1.37	1.19	0.08	0.11	0.34	2.91
Al ₂ O ₃	6.88	7.31	19.59	17.69	18.33	18.21	18.01	18.36	17.34	17.77	16.68	17.1	17.11	14.49	10.11
Fe ₂ O ₃	17.28	18.3	3.54	3.66	5.17	4.13	4.41	5.71	8	8.06	6.11	2.05	2.05	5.13	15.17
MnO	0.2	0.17	0.07	0.11	0.15	0.1	0.12	0.15	0.14	0.14	0.15	0.01	0.01	0.17	0.15
MgO	14.42	11.2	0.59	0.36	0.89	0.58	0.67	1.16	2.17	1.83	1.78	0.01	0.01	0.16	8.85
CaO	12.85	14.53	2.46	1.15	2.36	2.08	2.18	3.42	4.2	5.61	3.48	0.28	0.08	0.77	9.46
Na ₂ O	1.23	1.09	6.22	6.05	6.31	6.22	6.1	6.08	5.64	5.37	6.53	6.08	6.3	5.41	2.29
K ₂ O	0.4	0.35	4.33	5.53	4.2	4.64	4.58	3.47	3.59	2.63	4.07	5.71	5.66	4.79	0.16
P ₂ O ₅	0.45	0.15	0.12	0.06	0.24	0.12	0.14	0.31	0.6	0.59	0.26	0.01	0.02	0.03	0.47
LOI	-0.4	-0.2	1.28	0.42	0.37	0.79	0.65	0.2	0.78	0.19	0.85	0.39	0.33	0.46	3.44
Total	99.52	99.52	100.16	99.42	99.39	99.72	99.7	99.59	100.15	100.02	99.4	100.42	100.16	99.62	99.75
Mg-no.	64.8	57.4	26.8	17.8	27.5	23.6	25.1	30.9	37.4	33.3	39.1	1.1	1.1	6.4	56.2
Sc (ppm)	35.62	59.91	5.74	7.34	8.26	7.93	8.25	8.87	8.52	10.9	4.5	4.04	3.55	6.79	-
V	373.5	842.2	14.9	7.75	21.8	17.6	17.7	68.7	26.3	53.3	88	4.53	4.64	5.56	260
Cr	611	177.9	12.6	12.8	19.8	15.5	13.3	16.5	19.69	11.9	32	14.1	13.7	12.4	437
Co	85	86.92	3	1.78	4.17	3.1	5.29	14.3	5.48	12.1	19.4	0.62	0.82	1.2	61.6
Ni	388.9	204.4	3.47	3.13	7.16	7.1	7.25	13.3	9.12	2.81	21.2	1.53	0.94	1.97	246
Cu	88.68	60.72	-	-	-	-	-	-	-	-	-	-	-	-	-
Rb	9.27	8.67	56	84.8	66.3	62.4	64.9	88.7	50.2	57.19	168	92.9	94	144	20.4
Sr	668.6	546.4	638	170	599	525	493	736	776	893.7	1464	16.8	24.6	78.8	438.86
Y	19.99	17.13	20.1	33.7	33.2	25.1	26.9	35	30.7	44.3	25.8	28.5	41	72.8	28.29
Zr	181.1	169.2	337	614	466	591	529	323	297	447	479	340	564	1349	225.47
Nb	24.88	25.6	47.9	68.6	61	52.1	49.5	75.1	53.2	89.4	57.7	55.9	84.6	210	28.37
Ba	265.2	162.9	1538	1030	16121	1223	1185	1171	1884	891	1878	110	99.6	426	68.4
La	31.75	18.21	7.2	13.5	10.1	12.6	11.8	7.97	7.86	11.7	11.2	8.26	14.9	34.6	25.6
Ce	69.2	43.79	2.68	4.41	3.16	3.39	3.17	4.58	3.52	5.93	3.7	3.57	5.24	15.3	51.6
Pr	9.65	6.44	7.44	14.3	5.96	8.68	8.67	7.76	8.52	11.65	19.8	10	15.9	31.2	7.9
Nd	41.19	29.46	1.72	3.13	1.74	1.94	1.68	2.86	1.58	2.46	1.8	1.94	3.97	12.4	32.8
Sm	8.63	6.89	60.2	82.2	73.5	55	64.4	95.9	65.5	81.9	92.25	43.1	71.6	178	6.78
Eu	2.53	2.1	103	156	146	106	121	177	128	163	158.5	85	138.6	335	2
Gd	7.62	6.42	11.7	18.9	18.5	13	15.4	22	16.2	20.7	16.32	10.5	16.5	40.2	6.43
Tb	1	0.87	41.1	67	67.9	47.8	56.1	80.9	60.9	78.3	54.24	38.4	58	139	0.93
Dy	4.94	4.48	6.71	11.2	11.9	8.77	10.19	14	10.9	14.98	9.14	7.63	11.1	23.6	5.07
Ho	0.85	0.78	3.94	2.79	4.57	2.83	3.08	4.24	5.49	5.08	2.77	1.11	1.35	2.53	0.98
Er	1.91	1.69	5.68	9.13	9.88	7.14	8.38	11.7	8.96	13	6.84	6.72	9.85	19.5	2.44
Tm	0.23	0.21	0.82	1.36	1.48	1.11	1.25	1.69	1.37	1.95	1.06	1.09	1.65	2.98	0.36
Yb	1.36	1.24	4.35	7.25	7.43	5.62	6.27	8.33	6.96	10.4	4.99	5.71	8.82	15.9	1.77
Lu	0.19	0.18	0.76	1.26	1.29	0.98	1.14	1.38	1.23	1.85	0.95	1.01	1.58	2.89	0.25
Hf	4.98	4.94	1.93	3.23	3.24	2.48	2.84	3.39	3.02	4.57	2.35	2.59	4	7.63	5.37
Ta	1.79	1.88	0.25	0.43	0.41	0.33	0.37	0.42	0.39	0.6	0.38	0.36	0.53	1.06	1.95
Th	1.89	1.52	1.51	2.61	2.44	2.04	2.22	2.38	2.31	3.61	2.07	2.14	3.01	6.7	4.13
U	0.51	0.4	0.22	0.38	0.34	0.31	0.34	0.34	0.34	0.52	0.32	0.31	0.41	0.99	0.82
(La/Yb) _N	16.81	10.53	25.91	20.57	19.29	17.93	18.73	24.57	18.07	14.69	26.12	12.88	14.54	18.07	10.37
(Gd/Yb) _N	4.65	4.28	3.48	3.47	3.67	3.54	3.59	4.13	3.61	3.28	3.89	2.95	2.78	3.09	3.01
Eu/Eu*	0.95	0.97	1.95	0.84	1.29	1.09	1.02	1.01	1.70	1.11	1.07	0.47	0.39	0.36	0.93

Note: GB = Gabbro; CCP = Coarse-grained clinopyroxenite; OCP = Oxide clinopyroxenite; FCP = Fine-grained clinopyroxenite; OI-CP = Olivine clinopyroxenite; S = Syenite (data from Zhang et al., 2008); QS = Quartz syenite (data from Zhang et al., 2008); LOI = Loss on ignition. Mg-no. = [molar 100 × Mg/(Mg+Fe²⁺)], assuming 10% of total iron is ferric.

TiO₂ is consistent with compatible behavior of V in magnetite (Zhou et al., 2005; Fig. 4a). There are positive correlations of La and P₂O₅, Sc and Ni, and Zr and Nb among the rocks (Fig. 4b, c and d).

Olivine clinopyroxenite displays LREE-enriched patterns, with (La/Yb)_N ratios of 10.5–19.3 and (Gd/Yb)_N ratios of 4.1–4.7 (Fig. 5a) and weakly negative Eu anomalies (Eu/Eu* = 0.95–0.98). Similar REE patterns are observed for coarse-grained clinopyroxenites (Fig. 5c), but with relatively low REE concentrations. In contrast, fine-grained clinopyroxenite and oxide clinopyroxenite have lower REE concentrations and LREE-depleted (Fig. 5c) patterns with (La/Yb)_N ratio of 2.7–5.2. Gabbros have variable REE and moderately LREE-enriched patterns with (La/Yb)_N ratios of 13.0–24.9 and (Gd/Yb)_N ratios of 3.6–4.3 (Fig. 5e) and weakly negative to positive Eu anomalies (Eu/Eu* = 0.92–1.47, except one for 0.83). All the rocks from the mafic-ultramafic intrusion display positive Ba and Ti anomalies and negative Th, Zr and Hf anomalies on the primitive mantle-normalized trace element patterns (Fig. 5).

Syenites show highly LREE-enriched patterns with (La/Yb)_N ratios of 16.3–32 and (Gd/Yb)_N ratios of 2.7–4.1 (Fig. 5g). Quartz syenites have LREE-enriched patterns and relatively flat HREE patterns with (La/Yb)_N ratios of 14.4–19.1 and (Gd/Yb)_N ratios of 2.4–2.7 (Fig. 5g). Like gabbro, syenites commonly exhibit slightly positive Eu anomalies (Eu/Eu* ratios from 1.01 to 1.95), whereas quartz syenites display strong negative Eu anomalies (Eu/Eu* ratios from 0.36 to 0.47). On the primitive mantle-normalized trace element spiderdiagrams, syenite and quartz syenite show Sr and Ti depletions, whereas quartz syenite has strong negative Ba anomalies (Fig. 5).

5.3. Whole-rock Sr-Nd-Hf isotopes

The mafic-ultramafic rocks show restricted initial ⁸⁷Sr/⁸⁶Sr ratios ranging from 0.7037 to 0.7051. They have $\varepsilon_{\text{Nd}}(t)$ values ranging from +1.1 to +4.0 and $\varepsilon_{\text{Hf}}(t)$ values from 0.3 to 4.3 (Fig. 6 and Table 3). Syenite samples have initial ⁸⁷Sr/⁸⁶Sr ratios ranging from 0.7032 to 0.7037, much lower than quartz syenites (>0.7100). Syenite and quartz syenite have $\varepsilon_{\text{Nd}}(t)$ values (+1.44 to +2.92), virtually

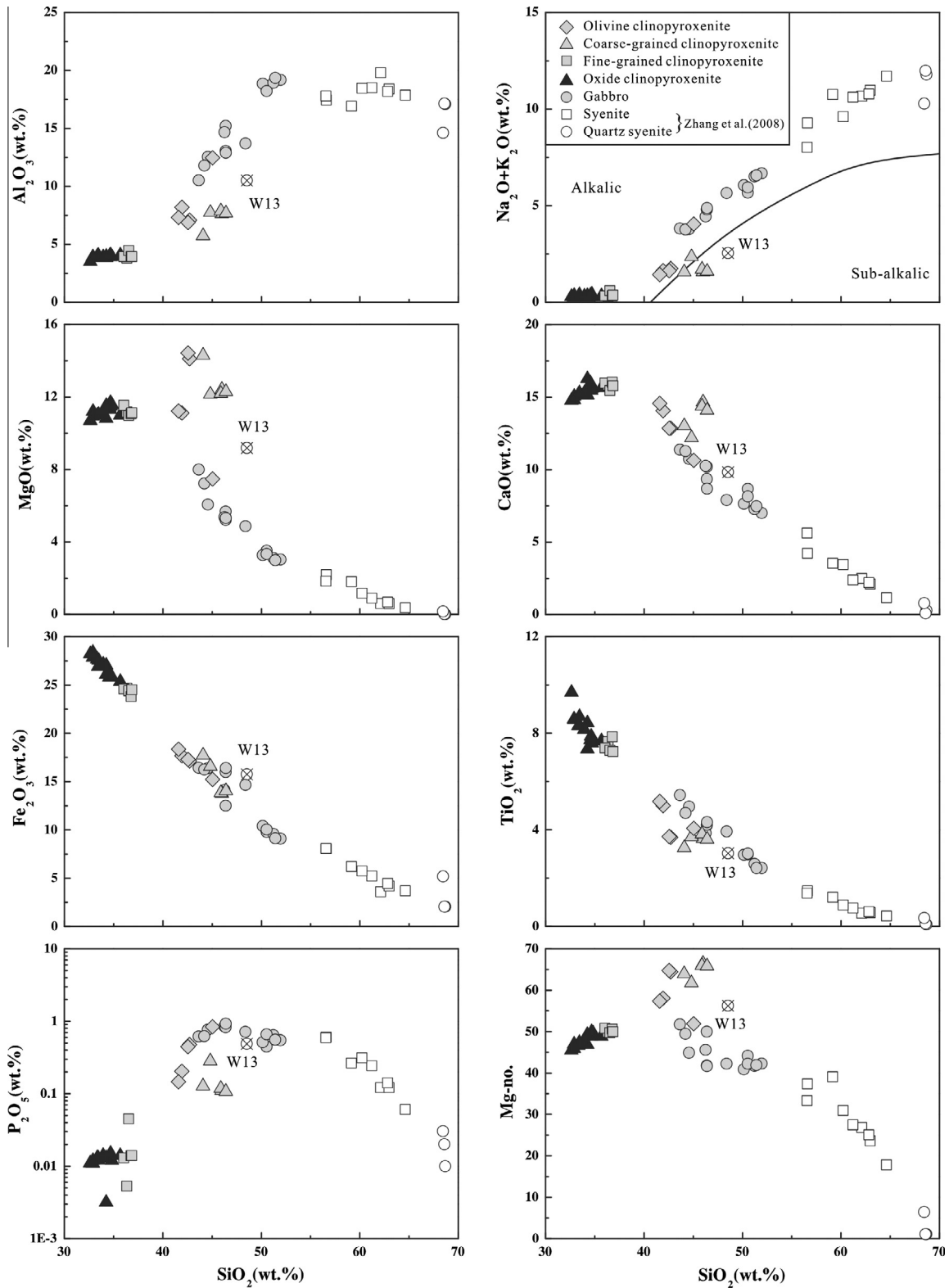


Fig. 3. SiO_2 versus Al_2O_3 , $\text{Na}_2\text{O} + \text{K}_2\text{O}$, MgO , CaO , Fe_2O_3 (as total iron), TiO_2 , P_2O_5 and Mg-no. for rocks from the Wajilitag complex. Data for the syenite and quartz syenite are from Zhang et al. (2008). All the values are normalized to 100% oxides free of LOI.

identical to the mafic-ultramafic rocks. The Sr-Nd-Hf isotopes of the Bachu mafic dykes and the Tarim basalts are also plotted in Fig. 6. Samples from the Wajilitag complex show isotopic characteristics similar to those of the Bachu mafic dykes (Fig. 6a and b), but display higher $\varepsilon_{\text{Nd}}(t)$, $\varepsilon_{\text{Hf}}(t)$ and lower initial $^{87}\text{Sr}/^{86}\text{Sr}$ values compared to the Tarim basalts (Fig. 6b).

5.4. Mineral compositions

5.4.1. Magnetite

Magnetite has $\text{Fe}_2\text{O}_3/\text{FeO}$ ratios ranging from 0.4 to 2.2 and TiO_2 from 0.2 to 24.2 wt.%, belonging to titanomagnetite (Supplementary Tables 1 and 2 and Fig. 7). Magnetite inclusions

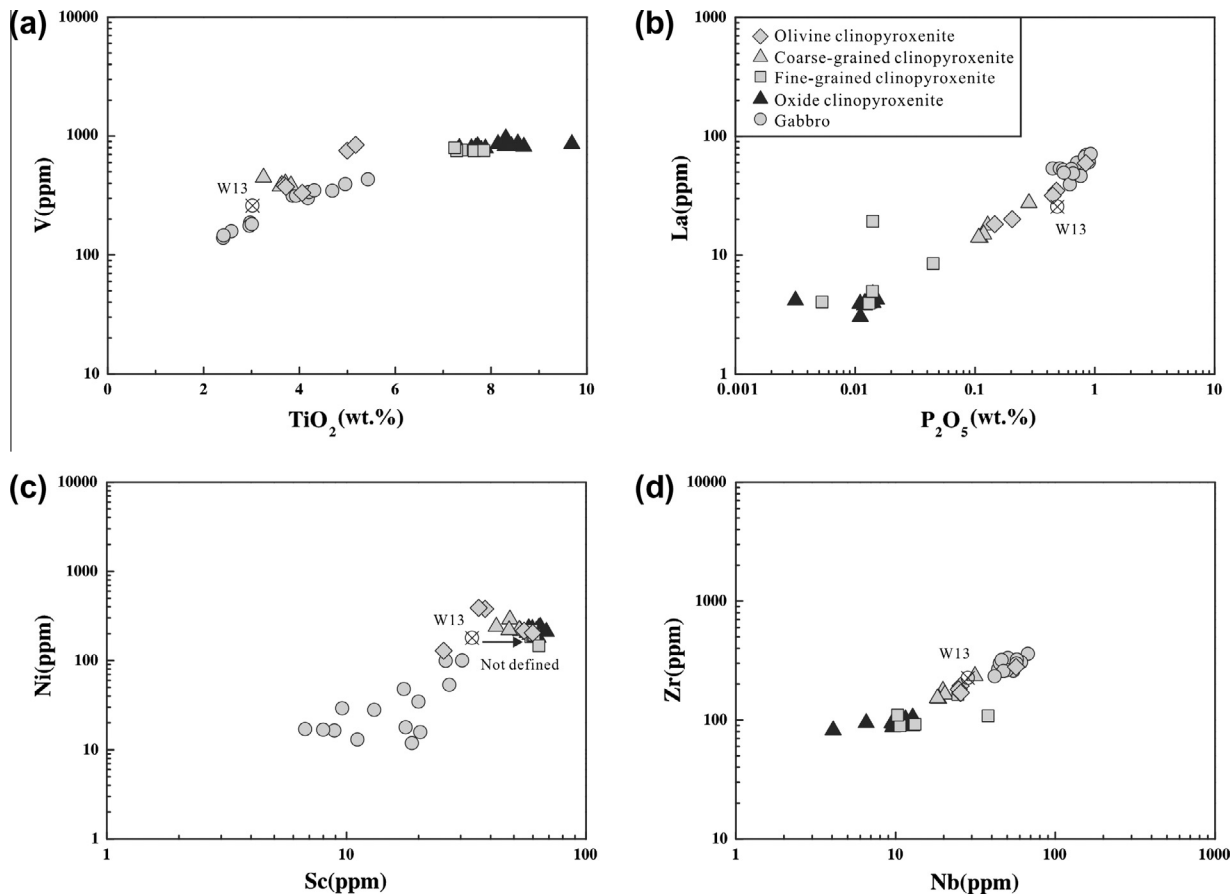


Fig. 4. Plots of V/TiO₂ versus MgO (a), La versus P₂O₅ (b), Ni versus Sc (c), Zr versus Nb (d) for the rocks from the Wajilitag layered intrusion.

in silicates of olivine clinopyroxenite have 33.9–41.5 wt.% FeO, 3.29–16.8 wt.% TiO₂ and 1.19–5.76 wt.% Cr₂O₃. Similar compositions are observed for magnetites enclosed in the minerals of coarse-grained clinopyroxenite (31.7–39.1 wt.% FeO, 0.67–11.0 wt.% TiO₂ and 1.31–12.5 wt.% Cr₂O₃). In contrast, interstitial magnetites in all the rock types have Cr₂O₃ lower than 0.97 wt.% (Fig. 7a–c). Specifically, interstitial magnetites in oxide clinopyroxenite have 1.99–5.47 wt.% Al₂O₃, 0.20–0.43 wt.% MnO and 1.29–4.74 wt.% MgO, higher than those of olivine clinopyroxenite, coarse-grained clinopyroxenite, fine-grained clinopyroxenite and gabbro.

5.4.2. Temperature and oxygen fugacity estimation

Compositions of coexisting titanomagnetite and ilmenite can be used to estimate the temperature and oxygen fugacity (f_{O_2}) at which these minerals last equilibrated (Buddington and Lindsley 1964). We performed the calculations on magnetite-ilmenite intergrowths using the ILMAT 2.0 by Lepage (2003) based on the geothermometer of Stormer (1983). The oxygen fugacities ($-\lg f_{\text{O}_2}$) obtained from the magnetite-ilmenite intergrowths range from 17.8 to 17.9 for olivine clinopyroxenite, which is similar to those for the coarse-grained clinopyroxenite (18.3–19.6) (Supplementary Table 3). The fine-grained clinopyroxenite and gabbro have higher estimates ranging from 20.9 to 25.1 and from 19.5 to 30.5, respectively. Oxide clinopyroxenite has relatively lower values (14.9–22.3). In a temperature versus $-\lg f_{\text{O}_2}$ diagram, all the rocks plot along the fayalite–magnetite–quartz (FMQ) curve (Fig. 8). The blocking temperatures of subsolidus equilibration in olivine clinopyroxenite vary from 664 to 671 °C, higher than those of coarse-grained clinopyroxenite (627–642 °C), fine-grained clinopyroxenite (543–623 °C) and gabbro (462–660 °C). All these blocking

temperatures are much lower than the crystallization temperature of magnetite and ilmenite (e.g., Vincent and Phillips, 1954), indicating a slow cooling process in the magma chamber in the formation of the intrusion.

5.4.3. Silicate minerals

Olivines from the Wajilitag mafic-ultramafic intrusion have Fo contents varying from 62 to 76 mol% (Supplementary Table 4), which is within the Fo range for the Panzhihua intrusion of the Emeishan LIP (28–82; Pang et al., 2009). The olivines in olivine clinopyroxenite (Fo = 71–76 mol%) have higher Fo content than those in coarse-grained clinopyroxenite (Fo = 62–70 mol%). The clinopyroxenes are augite and diopside (En_{36–43}Fs_{11–16}Wo_{45–49}) (Supplementary Table 5), similar to those reported from the Panzhihua intrusion (En_{32–54}Fs_{5–29}Wo_{40–44}; Pang et al., 2009). Clinopyroxenes from different clinopyroxenites have a similar mg-no. (73–82), and have higher MgO (13.2–15.3 wt%) and less FeO (6.2–9.0 wt%) and TiO₂ (0.5–2.3 wt%) than those from gabbros. FeO in clinopyroxenes decreases with increasing mg-no., indicating a fractionation trend (Fig. 9a–c). An content in plagioclase varies from 33 to 61 mol% (Supplementary Table 6; Fig. 9d), resembling those of the Panzhihua intrusion (An = 24–73; Pang et al., 2009). Plagioclase grains from olivine clinopyroxenite have the highest An contents.

Apatite from the Wajilitag layered intrusion is fluorapatite containing 1.2–2.6 wt.% F and <0.4 wt.% Cl (Supplementary Table 7). The calculated H₂O content vary between 0 and 0.4 wt%. The compositions of apatite are similar to cumulus apatite in the Panzhihua intrusion. Amphibole occurs as reaction rims of silicates in the gabbro and compositionally belongs to the kaersutite category. High H₂O content (up to 2 wt%) suggests that H₂O is the major volatile species in amphibole (Supplementary Table 7).

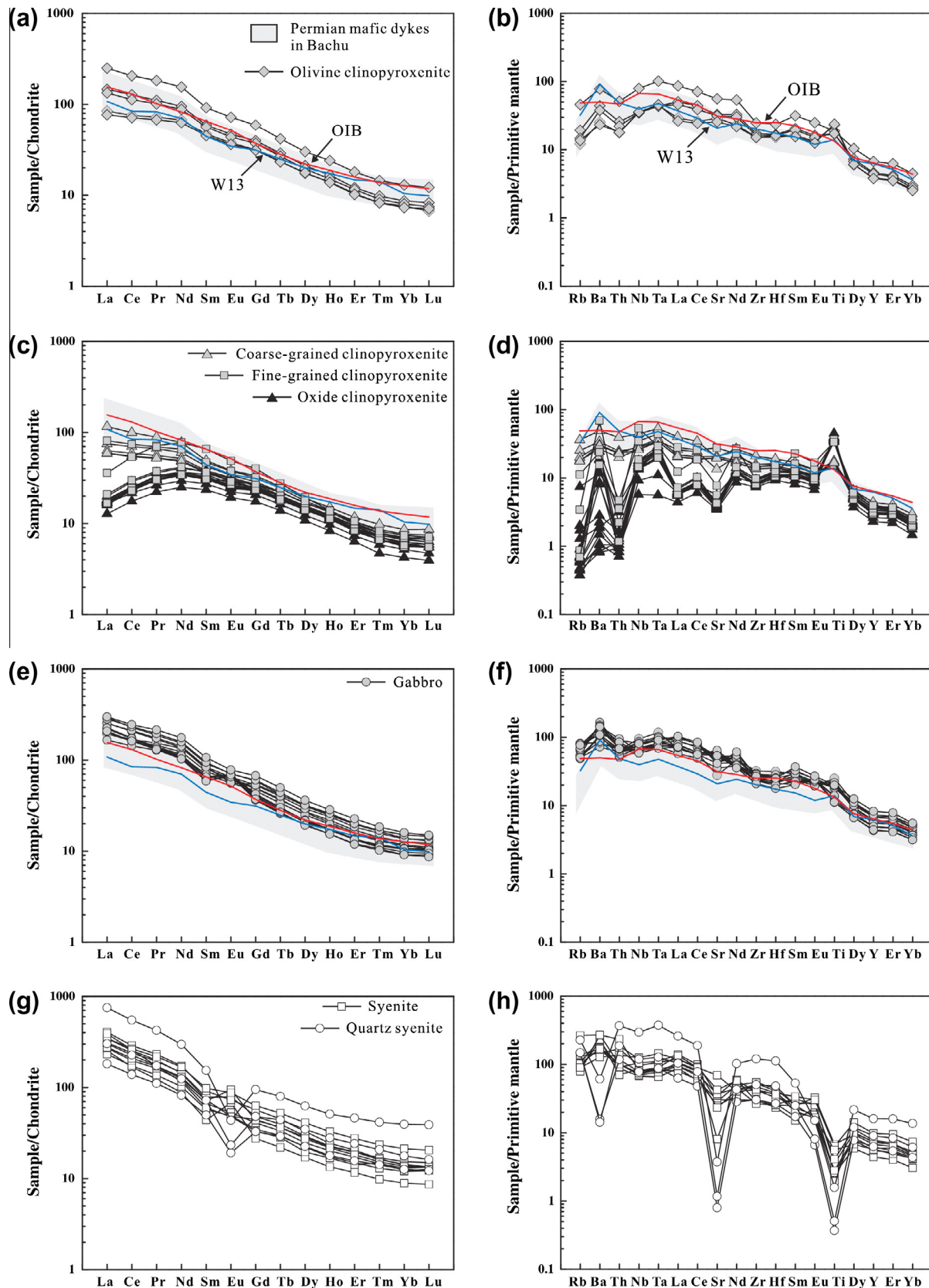


Fig. 5. Chondrite-normalized REE patterns and Primitive mantle-normalized trace element patterns of the rocks from the Wajilitag layered intrusion. All normalization values and OIB reference source are from Sun and McDonough (1989). Data for the mafic dykes are from Jiang et al. (2004a), Yang et al. (2007), Zhou et al. (2009) and Zhang et al. (2010c).

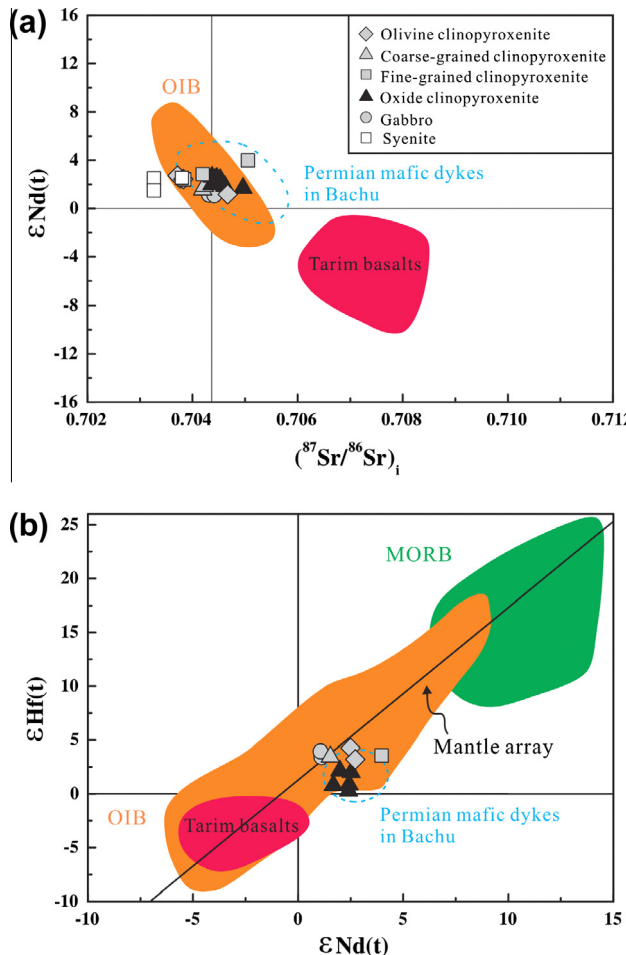


Fig. 6. (a) $\varepsilon_{\text{Nd}}(t)(t = 283 \text{ Ma})$ values versus initial $^{87}\text{Sr}/^{86}\text{Sr}$ diagram for the rocks from the Wajilitag complex. (b) $\varepsilon_{\text{Hf}}(t)$ versus $\varepsilon_{\text{Nd}}(t)$ diagram for the mafic-ultramafic rocks. Data for the mafic dykes in Bachu are from Jiang et al. (2004a), Yang et al. (2007), Zhou et al. (2009) and Zhang et al. (2010a). Data for the Tarim basalts are from Li et al. (2012b), Yu et al. (2011) and Zhou et al. (2009). The initial $^{87}\text{Sr}/^{86}\text{Sr}$, $\varepsilon_{\text{Nd}}(t)$ and $\varepsilon_{\text{Hf}}(t)$ are calculated at $t = 283 \text{ Ma}$ for the Wajilitag complex and mafic dykes, and $t = 289 \text{ Ma}$ for the Tarim basalts, respectively. The OIB and MORB fields being from Salters (1996) and Wilson (1989). The OIB array being from Chauvel et al. (2008).

6. Discussion

6.1. Petrogenesis of the Wajilitag complex

6.1.1. Mafic-ultramafic intrusions

The mafic-ultramafic and syenitic rocks of the Wajilitag Complex have LREE-enriched patterns and slightly negative Nb and Ta anomalies (Fig. 5), which may be attributed to crustal contamination. However, high degrees of crustal contamination usually accompany enrichment of Zr and Hf, which are not observed for the Wajilitag complex (Fig. 5b, d, f and h). Th/Ta ratio is a sensitive indicator of crust contamination (Shellnutt et al., 2009). Th/Ta ratios of the rocks from the Wajilitag complex vary from 0.06 to 5.35 with an average of 1.29, similar to that for the mantle-derived rocks (Th/Ta = 2, Shellnutt et al., 2009), but much lower than the continental lower crust (Th/Ta = 7.9) or upper continental crust (Th/Ta = 6.9). Mantle-derived magmas that assimilated significant crustal material should result in enrichment of radiogenic Nd and hence low Nd. The Wajilitag complex displays a limited range of positive $\varepsilon_{\text{Nd}}(t)$ values (+1.1 to +4.0), inconsistent with that expected by crustal contamination (Fig. 6). Therefore, trace elements,

and Sr and Nd isotopes are not supportive of significant crustal contamination during the formation of the Wajilitag complex.

Elemental ratios such as Th/U and Zr/Nb are commonly used for fingerprinting the nature of the mantle source from which the rocks were derived (Eby, 1998; Shellnutt et al., 2009). The Th/U and Zr/Nb ratios of the Wajilitag mafic-ultramafic rocks mostly vary from 0.3 to 5.5, and from 2.9 to 10.6, respectively. These ratios are comparable with those of OIB (Th/U = 3.5–3.8, Weaver, 1990; Zr/Nb < 10, Pearce and Norry, 1979). In addition, the mafic-ultramafic rocks display trace element patterns similar to oceanic island basalts (OIB) (Fig. 5). Their initial $^{87}\text{Sr}/^{86}\text{Sr}$ ratios (0.7037–0.7051) and $\varepsilon_{\text{Nd}}(t)$ (0.97–3.9) also resemble an OIB enriched mantle source (Fig. 6a and b). This type of mantle source resembles that of many primary oceanic and continental alkaline suites which also possess positive $\varepsilon_{\text{Nd}}(t)$ in association with LREE enrichment, and provides evidence for an OIB-like, asthenospheric mantle source (Hou et al., 2012).

The mafic-ultramafic rocks of the Wajilitag complex have trace element patterns and $\varepsilon_{\text{Nd}}(t)$ values similar to the mafic dykes in the Bachu region (Fig. 6a and b), indicating that they may share a similar mantle source (Jiang et al., 2004a; Zhou et al., 2009; Zhang et al., 2010a). However, they are isotopically different from the Tarim flood basalts, which have much lower $\varepsilon_{\text{Nd}}(t)$, $\varepsilon_{\text{Hf}}(t)$ and higher initial $^{87}\text{Sr}/^{86}\text{Sr}$ values (Fig. 6). It has been argued that the Tarim basalts, which were mainly emplaced at ~290 Ma, were likely derived from a subcontinental lithospheric mantle source metasomatized by subduction-related processes (Li et al., 2012b). The shift of magma source in the Tarim LIP from lithospheric mantle (~290 Ma) to asthenosphere (~280 Ma) is attributable to plume incubation under the thick Tarim craton, followed by deflection of the plume towards the cratonic margins with thin lithosphere (Xu et al., 2013; Wei et al., 2013).

6.1.2. Syenitic plutons

At Wajilitag, the syenitic plutons are spatially associated with the mafic-ultramafic intrusion so that these two members are likely coeval. This is consistent with lack of field evidence that the syenites were formed later than the layered intrusion. However, currently available zircon U-Pb dating reveals an age gap of ~9 Ma between them (Zhang et al., 2008; Huang et al., 2012). Although additional chronological studies are needed in the future to solve this problem, we consider these syenites an integral part of the Tarim LIP because their emplacement ages are within the second episode of Tarim magmatism (Wei et al., 2013).

Syenitic magmas can be produced by partial melting or fractional crystallization of mantle-derived mafic rocks or by remelting of crustal rocks (Collins et al., 1982; Clemens et al., 1986; Eby, 1990, 1992; Frost and Frost, 1997; Shellnutt and Zhou, 2007; Zhong et al., 2009). The syenite and quartz syenite at Wajilitag have Th/U and Zr/Nb ratios ranging from 2.5 to 11, and from 4.3 to 11.3. Their $\varepsilon_{\text{Nd}}(t)$ values vary from +1.3 to +2.8, close to those of the mafic-ultramafic rocks. This, together with their close spatial association, implies that they may have been derived from the same mantle source. If this is the case, it is unlikely that the syenites formed from melting of ancient crystalline basement. A more likely scenario is that the syenites were generated from mafic rocks either by partial melting or by fractional crystallization. The co-variation of compatible element versus incompatible element is a powerful tool to discriminate between fractional crystallization and partial melting processes (Peccerillo et al., 2003). Geochemical modeling shows that the low Sr and V in the syenites cannot be explained by a single-stage partial melting of mafic rocks (Fig. 10); in contrast, these variations can be obtained by fractional crystallization starting from the average composition of the coeval Bachu mafic dykes having mg-no. > 50 ($n = 7$; Jiang et al., 2004a; Zhou et al., 2009). Thus, the syenites are interpreted as results of fractional

Table 3

Rb–Sr, Sm–Nd and Lu–Hf radiogenic isotope data for the mafic-ultramafic rocks.

Sample no.	Rock type	Rb (ppm)	Sr (ppm)	$^{87}\text{Rb}/^{86}\text{Sr}$	$^{87}\text{Sr}/^{86}\text{Sr}$	$\pm 2\sigma$	$(^{87}\text{Sr}/^{86}\text{Sr})_i$ (283Ma)	Sm (ppm)	Nd (ppm)	$^{147}\text{Sm}/^{144}\text{Nd}$	$^{143}\text{Nd}/^{144}\text{Nd}$	$\pm 2\sigma$
BC1102	Gabbro	32.04	873.8	0.1061	0.70473	0.000013	0.70430	11.49	57.65	0.120491	0.512591	0.000005
BC1103	Gabbro	51.32	583.3	0.2545	0.70534	0.000013	0.70432	12.9	63.03	0.12373	0.512559	0.000007
BC1104	Gabbro	33.93	743.7	0.132	0.70495	0.000012	0.70442	10.61	51.4	0.124791	0.512558	0.000007
BC1116	Coarse-grained clinopyroxenite	11.45	412.8	0.0802	0.70452	0.000012	0.70420	5.664	22.87	0.149726	0.512634	0.000006
BC1119	Coarse-grained clinopyroxenite	11.15	410.9	0.0785	0.70454	0.000011	0.70422	5.469	22.5	0.146948	0.512641	0.000005
BC1123	Oxide clinopyroxenite	0.238	75.73	0.0091	0.70441	0.000014	0.70437	4.892	16.39	0.180449	0.512712	0.000006
BC1124	Oxide clinopyroxenite	0.372	79.27	0.0136	0.70467	0.000012	0.70462	4.704	15.84	0.179539	0.512702	0.000012
BC1126	Oxide clinopyroxenite	0.657	95.89	0.0198	0.70451	0.000012	0.70443	5.733	21.98	0.157688	0.512686	0.000005
BC1128	Oxide clinopyroxenite	0.304	90.25	0.0097	0.70441	0.000013	0.70437	5.248	17.17	0.184788	0.512746	0.000004
BC1131	Oxide clinopyroxenite	1.247	99.16	0.0364	0.70461	0.000013	0.70446	5.076	18.53	0.165612	0.512707	0.000007
BC1140	Oxide clinopyroxenite	0.24	86.7	0.008	0.70456	0.000012	0.70453	4.806	16.17	0.179689	0.512731	0.000006
BC1146	Oxide clinopyroxenite	4.72	75.23	0.1815	0.70569	0.000019	0.70496	4.181	13.76	0.183699	0.512697	0.000007
BC1141	Fine-grained clinopyroxenite	2.182	163.7	0.0386	0.70435	0.000012	0.70420	10.07	36.24	0.167992	0.512729	0.000007
BC1148	Fine-grained clinopyroxenite	7.13	581.3	0.0355	0.7052	0.000011	0.70506	7.156	30.52	0.141754	0.512739	0.000006
BC1171	Olivine clinopyroxenite	12.27	695.5	0.051	0.70397	0.000014	0.70377	9.09	44.56	0.123327	0.512630	0.000006
BC1172	Olivine clinopyroxenite	29.39	1180.7	0.072	0.70496	0.000013	0.70467	14.09	72.88	0.116878	0.512550	0.000007
BC1173	Olivine clinopyroxenite	7.685	614.2	0.0362	0.70386	0.000012	0.70371	7.209	31.43	0.138667	0.512668	0.000007
BC1175	Olivine clinopyroxenite	8.667	546.4	0.0459	0.70401	0.000014	0.70383	6.893	29.46	0.141454	0.512656	0.000007
$(^{143}\text{Nd}/^{144}\text{Nd})_i$ (283Ma)	$\varepsilon_{\text{Nd}}(t)$	Lu (ppm)	Hf (ppm)	$^{176}\text{Lu}/^{177}\text{Hf}$	$^{176}\text{Hf}/^{177}\text{Hf}$		$(^{176}\text{Hf}/^{177}\text{Hf})_i$ (283Ma)	$\pm 2\sigma$	$\varepsilon_{\text{Hf}}(t)$			
0.512367	1.8											
0.512331	1.1	0.368	9.714	0.00537	0.28272	0.28269		0.000007	3.4			
0.512329	1.1	0.268	7.204	0.00527	0.28273	0.28271		0.000007	3.9			
0.512353	1.5	0.159	4.311	0.00523	0.28272	0.28269		0.000007	3.5			
0.512368	1.8											
0.512376	2.0	0.139	3.359	0.00587	0.28269	0.28266		0.000007	2.2			
0.512367	1.8											
0.512398	2.4	0.144	3.247	0.00629	0.28265	0.28262		0.000010	0.9			
0.512408	2.6											
0.512403	2.5	0.139	3.364	0.00586	0.28268	0.28265		0.000009	2.0			
0.512397	2.4	0.137	3.321	0.00585	0.28263	0.28260		0.000009	0.3			
0.512360	1.7	0.121	3.538	0.00485	0.28264	0.28262		0.000008	0.8			
0.512419	2.8											
0.512477	4.0	0.176	4.791	0.00521	0.28272	0.28270		0.000007	3.6			
0.512402	2.5	0.206	5.116	0.00571	0.28275	0.28272		0.000006	4.3			
0.512333	1.2											
0.512413	2.7	0.174	4.691	0.00526	0.28271	0.28269		0.000006	3.2			
0.512398	2.4											

crystallization of basaltic parental magma. In addition, the Tzr values for the syenites range from 843 to 981 °C, consistent with those of basaltic magma-fractionated A-type granites in the Emeishan LIP (Zhong et al., 2007).

However, the lack of reciprocal patterns (e.g., Eu, ΣREE, Zr, Hf) between syenites and layered mafic-ultramafic intrusion in trace element distribution patterns (Fig. 5) argues against a direct derivation of the Wajilitag syenites from differentiation of the layered mafic-ultramafic intrusion. As described above, the mafic-ultramafic rocks are generally characterized by negative Th and Zr–Hf anomalies (Fig. 5). This is consistent with the fact that Zr, Hf and Th behave incompatibly in mafic rock system. The syenites exhibit no Th and Zr–Hf depletions, resembling the Panzhihua syenites in the Emeishan LIP (Shellnutt et al., 2007; Zhong et al., 2009). Following Zhong et al. (2009), we propose that the Wajilitag syenites were generated by the emplacement of syenitic melts from differentiation of newly underplated basaltic magmas at depth and subsequent fractional crystallization.

Syenite and quartz syenite have good linear correlations of CaO, Fe₂O₃, Al₂O₃ and Na₂O + K₂O against SiO₂, indicating a fractionation trend. It is likely that fractionation of syenites led to the formation of quartz syenites. The systematic decrease in TiO₂, MgO,

Fe₂O₃, CaO, P₂O₅ contents with increasing SiO₂ can be accounted for by fractionation of mafic minerals, Fe–Ti oxides, feldspars and apatite (Fig. 3). Variably positive Eu anomalies in the syenite could be attributed to accumulation of plagioclase. In contrast, the strong depletions in Sr and Ba in quartz syenite (Fig. 5h) are indicative of fractionation of feldspars.

6.2. Formation of Fe–Ti oxide deposits

Formation of Fe–Ti oxide deposits in layered intrusions may be controlled by several parameters, including composition of parental magma, fractionation processes and oxygen fugacity. In the following these parameters will be evaluated in detail with aims of better understanding the conditions and mechanism under/by which the Wajilitag Fe–Ti oxide ore deposits were formed.

6.2.1. Parental magma

A Fe-and Ti-rich parental magma that generated the Wajilitag layered intrusion is suggested by enrichment of Fe and Ti in the Wajilitag complex, and by the presence of ilmenite exsolution lamellae in clinopyroxene and Ti-rich clinopyroxene. Using MgO–FeO correlation in the olivine clinopyroxenite and the composition

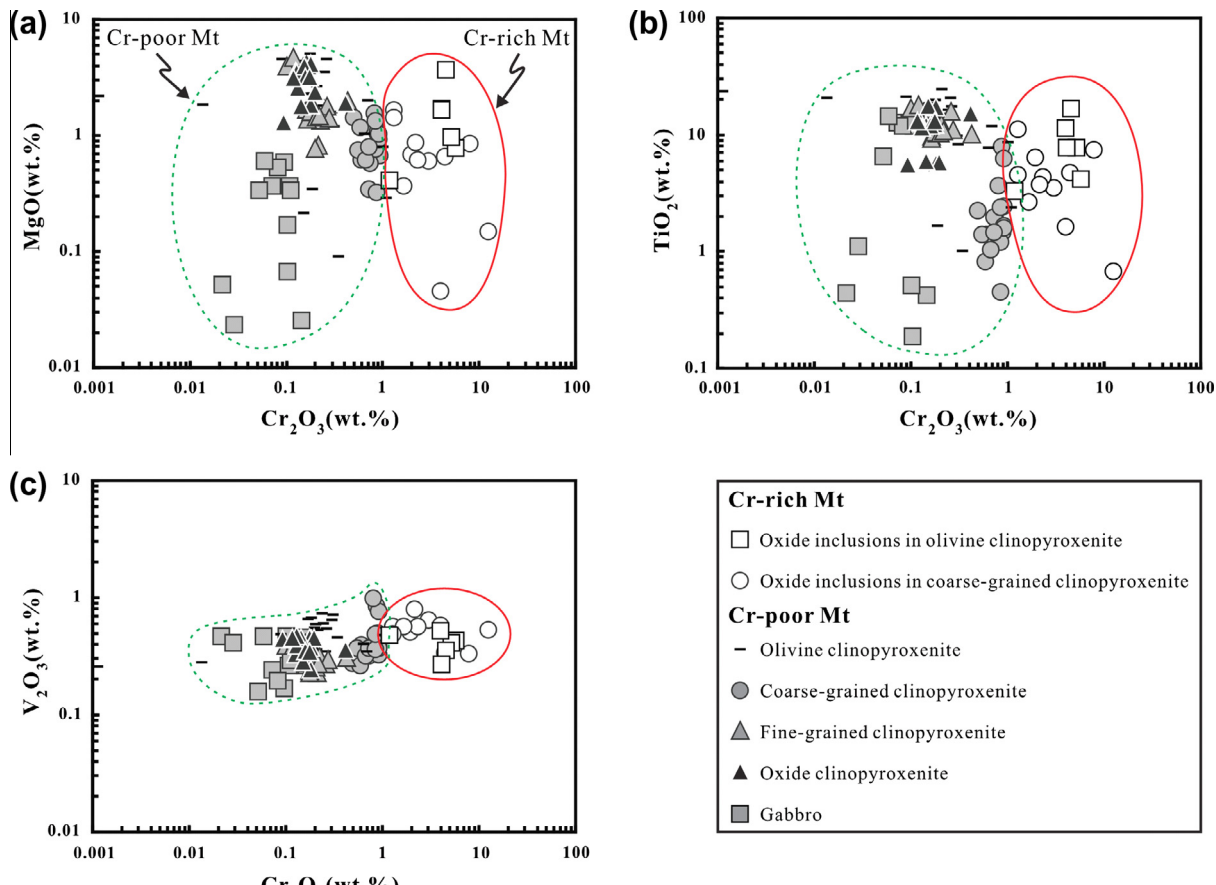


Fig. 7. Plots of Cr_2O_3 versus MgO , TiO_2 and V_2O_3 for titanomagnetites from the Wajilitag layered mafic-ultramafic intrusion.

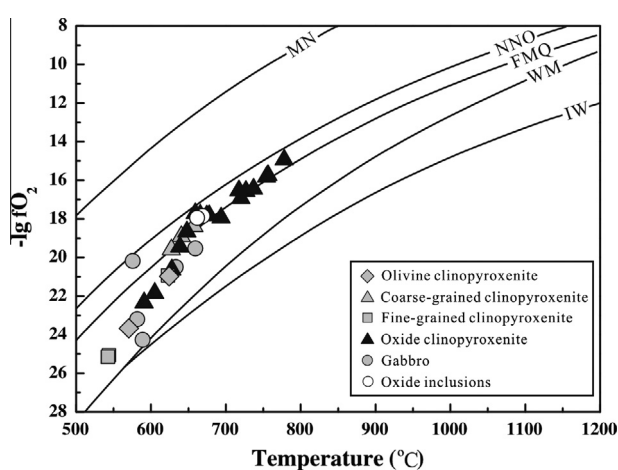


Fig. 8. Oxygen fugacity and temperature determined for the Wajilitag intrusion based on magnetite-ilmenite reequilibration. MN trajectory for magnetite-nickel buffer, NNO for nickel-nickel-oxide, FMQ for quartz-fayalite-magnetite, WM for wüstite-magnetite and IW for iron-wüstite (Eugster and Wones, 1962).

of the most magnesian olivine ($\text{Fo} = 76$) from this unit, the parental magma from which olivine crystallized is estimated to have a Mg-no. of 49. In our calculation, it is assumed that samples represent olivine–melt mixtures at magmatic temperatures and the Mg–Fe exchange coefficient between olivine and melt is 0.3 (Roeder and Emslie, 1970). The estimated compositions of parental magmas are comparable with the high-Mg mafic dike sample W13, which is the least fractionated one (Mg-no. = 50–56) in this region (Jiang

et al., 2004a; Zhou et al., 2009). As suggested by Zhang et al. (2008), the sample W13 can be regarded as the parental magmas of the alkaline mafic-ultramafic rocks in the Wajilitag complex.

Low Fo contents (62–76) in olivines (Supplementary Table 4) from the Wajilitag mafic-ultramafic intrusions may indicate that the parental magma of the intrusion is much evolved. It is likely that an ultramafic portion may have been left in a deep-seated chamber while residual melts rise to a shallow chamber to form the Wajilitag mafic-ultramafic intrusions.

6.2.2. Fractionation of Fe-Ti-rich parental magma and magnetite accumulation

Many classic layered mafic intrusions in the world, such as Skaergaard and Kiglapait intrusions, have long been thought to represent products of closed magmatic system that involved differentiation of a single pulse of magma (Wager and Brown, 1968). Given the good correlation between major elements (Fig. 3), we consider that the Wajilitag mafic-ultramafic intrusion may also be formed from a single pulse of evolved magmas. The overlapping and largely uniform mineral compositions and similar Sr–Nd isotopes of different rock types further indicate the Wajilitag layered intrusion formed from a common differentiating magma. Nevertheless, we cannot preclude the possibility that the intrusion may have been recharged at a deeper level because the floor of the intrusion has not yet been exposed. Fe-Ti oxide inclusions in olivine or clinopyroxene have higher Cr_2O_3 content than interstitial Fe-Ti oxides. This may reflect a two-stage fractionation process of an Fe-Ti-rich parental magma. Cr has a high partition coefficient in Cr-Fe-Ti oxides, like magnetite, during fractionation of magmas ($D_{\text{Cr}}^{\text{magnetite/melt}} = 100 - 620$, McCarthy et al., 1985), therefore Cr-rich

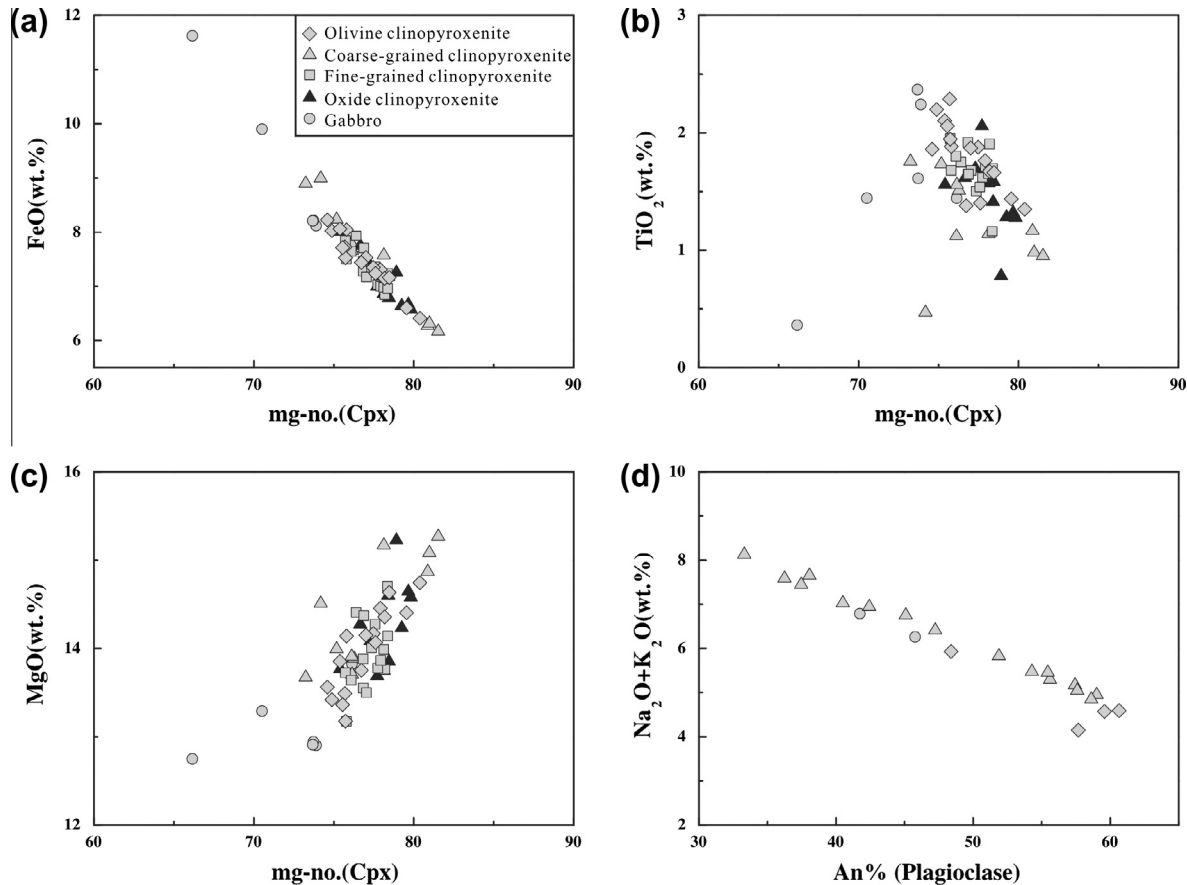


Fig. 9. Plots of mg-no. versus FeO, TiO₂, MgO (wt.%) in clinopyroxenes and An versus Na₂O + K₂O (wt.%) in plagioclase for the Wajilitag layered intrusion.

titanomagnetite represents an early crystallization phase, whereas large amounts of Cr-poor titanomagnetite formed from more evolved residual magmas that percolated through silicate crystal mush. In this fashion, Cr-rich and Cr-poor titanomagnetite formed in early and later stages from a continuous fractionation process. Given the absence of conjugate felsic rocks at Wajilitag, We think liquid immiscibility may not have happened during the evolution of magmas, as was invoked for the Hongge intrusion of the Emeishan LIP (Wang and Zhou, 2013).

The MELTS program of Ghiorso and Sack (1995) is used to understand the fractionation process associated with the Wajilitag complex. The most primitive mafic dike sample (W13) is assumed as the parental magma of the Wajilitag mafic-ultramafic intrusion, and calculation is simulated for a system with 1.5 wt.% H₂O at 1 kbar and FMQ + 1 buffer. The modeling results indicate that the sequence of mineral crystallization (olivine → clinopyroxene → Fe-Ti oxides → plagioclase) is generally consistent with petrographic observations. Notably, the modeling also predicts the onset of Fe-Ti spinel crystallization at 1114 °C, which clearly demonstrates the early saturation of Fe-Ti oxides in the magma evolution (Fig. 11).

6.2.3. Factors controlling the saturation of Fe-Ti oxide saturation

The temperature at the onset of Fe-Ti oxide crystallization is in part positively correlated with FeO and TiO₂ contents and negatively correlated with SiO₂ content of the magma (Toplis and Carroll, 1995). The parental magma composition of the Wajilitag mafic-ultramafic intrusions as discussed above is rich in Fe and Ti but relatively poor in SiO₂. Therefore early crystallization of Fe-Ti oxides can be in part attributed to the compositional characteristics of the parental magma.

Melting experiments in ferrobasaltic system at low pressure indicate that Fe-Ti oxide crystallization is enhanced under relatively high fO₂ (Toplis and Carroll, 1995). Periodic fluctuation of fO₂ in the magma has been invoked as the mechanism for the formation of titanomagnetite layers in the Upper Zone of the Bushveld Complex (Klemm et al., 1985). Vanadium in magnetite is an excellent fractionation index (Toplis and Corrane, 2002) and the distribution coefficient of V between magnetite and silicate melts ($D_V^{Mt/liq}$) strongly depends on fO₂ (Canil, 1999; Toplis and Corrane, 2002). As a result, the distribution coefficient of this element between magnetite and melts in the Wajilitag layered intrusion can be used as an indicator of fO₂ during its crystallization.

$D_V^{Mt/liq}$ for Cr-poor titanomagnetite is estimated based on a linear trend of V partitioning between magnetite and melt. fO₂ can be expressed by the equation: $D_V^{Mt/liq} = V_{magnetite}/V_{magma} = -9.39 \times (\Delta FMQ) + 37.45$ (Toplis and Corrane, 2002). Assuming that the parental magma of the Wajilitag mafic-ultramafic rocks contains 244 ppm V, a value similar to the averaged V concentration of the mafic dikes in the Bachu region (Jiang et al., 2004a; Zhou et al., 2009), the estimated fO₂ values of the magma vary from FMQ + 1.1 to FMQ + 3.5. It means that abundant magnetite grains crystallized from the magma when the fO₂ reaches FMQ + 1.1 to FMQ + 3.5. On the other hand, coexistence of sulfides with Fe-Ti oxides in the Wajilitag layered intrusion may indicate that the oxidation state at magmatic temperatures was no more than FMQ + 2 (Bai et al., 2012). So fO₂ during Fe-Ti oxide crystallization is estimated to be FMQ + 1.1 to FMQ + 2 in the Wajilitag case. Similar values have been obtained for the Hongge and Panzhihua intrusions of the Emeishan LIP (Pang et al., 2009; Bai et al., 2012). Interstitial Cr-poor titanomagnetite grains in the Wajilitag layered

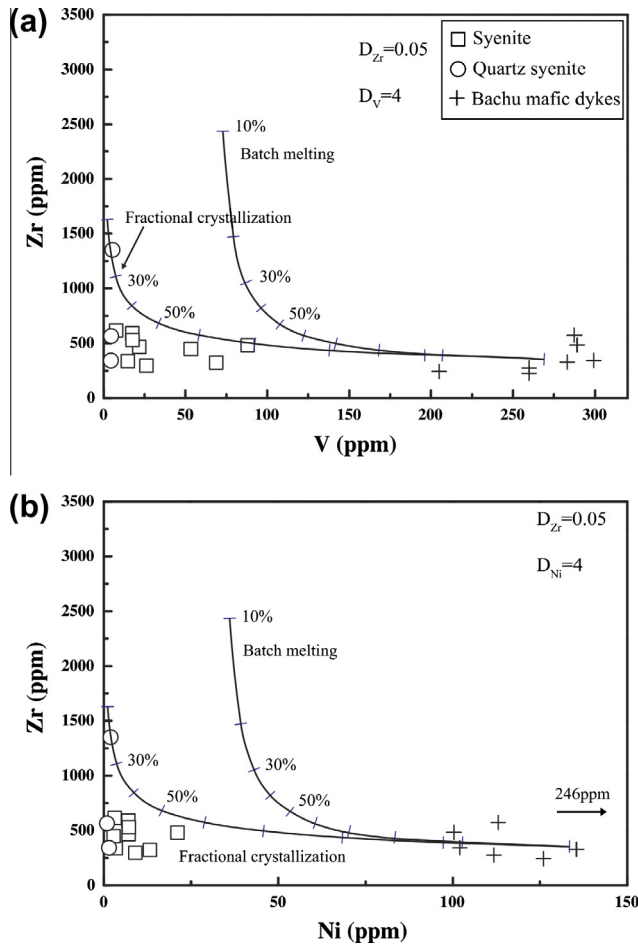


Fig. 10. Compatible versus incompatible trace elements for the Wajilitag syenitic rocks. The average composition of Bachu mafic dykes ($Mg\text{-no.} > 50$; Jiang et al., 2004a; Zhou et al., 2009) is assumed as the starting composition for both batch melting and fractional crystallization. Partition coefficients are similar to those of Peccerillo et al. (2003).

intrusion have lower V_2O_3 contents than Cr-rich titanomagnetite (Fig. 3c), consistent with crystallization under a higher fO_2 condition. The Fe_2O_3 content of the magma in the Wajilitag layered intrusion can also be elevated with the crystallization of silicate minerals. This is evidenced by the higher $Fe^{3+}/(Fe^{3+}+Fe^{2+})$ in oxide clinopyroxenite, compared with those in other rock types of the layered intrusion (Supplementary Table 5). The presence of amphibole and apatite (Fig. 2g; Supplementary Table 7) supports the idea that the amounts of volatile and P are elevated in the residual liquid.

6.2.4. Formation of Fe-Ti oxide ores

In the Wajilitag layered intrusion, minor Cr-rich magnetites, which occur in olivine clinopyroxenite and coarse-grained clinopyroxenite in the lower part of the sequence, are not major part of Fe-Ti oxide ores, whereas Cr-poor magnetites that occur in oxide clinopyroxenite and fine-grained clinopyroxenite in the upper part of the intrusion makes up the major ore bodies. As stated above, Cr-rich and Cr-poor titanomagnetites were formed in early and late stages, respectively, of a continuous fractionation process. Crystallization of large amounts of silicate minerals increases the FeO and TiO_2 contents, fO_2 and volatile contents of the residual magmas, which are favorable for mass crystallization of Fe-Ti oxide minerals. Once Fe-Ti oxide minerals formed, due to their high density, they would settle downward and percolate through the crystal

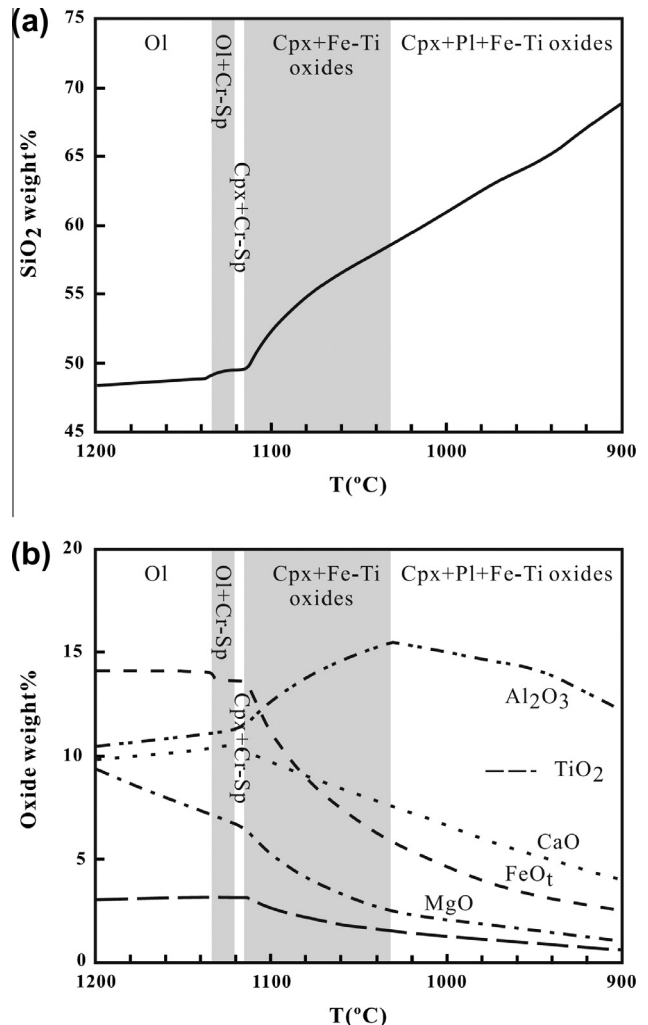


Fig. 11. Results of MELTS modeling using a starting composition of high-Mg mafic dyke sample W13 and assuming $fO_2 = FMQ + 1$ buffer, starting temperature of 1200 °C, ending temperature of 900 °C, $H_2O = 1.5$ wt.% and pressure of 1000 bars.

mush in a slowly cooling magma chamber as reflected by the low blocking temperatures (Fig. 8). In this scenario, oxide clinopyroxenite and fine-grained clinopyroxenite could have been produced by infiltration of Fe-Ti oxide minerals into the early unconsolidated clinopyroxene-dominated cumulates, similar to the model proposed for the net-textured ores composed of olivine, plagioclase, Fe-Ti oxide, and apatite in the upper zone of the Bushveld Complex (von Gruenewaldt, 1993).

7. Conclusions

The Wajilitag complex, which is composed of the layered mafic-ultramafic intrusion and syenitic plutons, is part of the Tarim LIP. The complex was derived from an enriched plume mantle source and the layered mafic-ultramafic intrusion formed from an Fe-Ti-rich basaltic magma. Major Fe-Ti oxide mineralization occurred when large amounts of Cr-poor magnetite crystallized from more evolved magmas that percolated through crystal mush under high fO_2 and a volatile-rich condition during the late-stage of magmatic differentiation. Syenite may have formed by differentiation of underplated magmas at depth which share the same parental magmas with the layered mafic-ultramafic intrusion. Quartz syenite represents residual melts after fractional crystallization of syenitic melts during ascent.

Acknowledgements

Drs. Zhenyu Luo, Haiquan Liu and Linli Chen are thanked for their laboratory assistance. Journal reviews by Andy Saunders and an anonymous reviewer, and comments from the guest editor Hetu Sheth have significantly improved the paper. This study is supported by the 973 project (2011CB808906) and GIG-CAS 135 project (Y234051001). This is contribution No IS-1741 from GIG-CAS.

Appendix A. Supplementary data

Supplementary data associated with this article can be found, in the online version, at <http://dx.doi.org/10.1016/j.jseas.2013.09.014>.

References

- Bai, Z.-J., Zhong, H., Naldrett, A.J., Zhu, W.-G., Xu, G.-W., 2012. Whole-rock and mineral composition constraints on the genesis of the giant Hongge Fe-Ti-V oxide deposit in the Emeishan Large Igneous Province, southwest China. *Economic Geology* 107, 507–524.
- Bernstein, S., Kelemen, P.B., Brooks, C.K., 1996. Evolution of the Kap Edward/Holm Complex: a mafic intrusion at a rifted continental margin. *Journal of Petrology* 37, 497–519.
- Bryan, S.E., Ernst, R.E., 2008. Revised definition of Large Igneous Provinces (LIPs). *Earth Sciences Review* 86 (1–4), 175–202.
- Buddington, A.F., Lindsley, D.H., 1964. Iron-titanium oxide minerals and synthetic equivalents. *Journal of Petrology* 5, 310–357.
- Carmichael, I.S.E., 1967. The iron-titanium oxides of salic volcanic rocks and their associated ferromagnesian silicates. *Contributions to Mineralogy and Petrology* 14, 36–64.
- Canil, D., 1999. Vanadium partitioning between orthopyroxene, spinel and silicate melt and the redox states of mantle source regions for primary magmas. *Geochimica et Cosmochimica Acta* 63, 557–572.
- Chauvel, C., Lewin, E., Carpentier, M., Arndt, N.T., Marini, J.C., 2008. Role of recycled oceanic basalts and sediment in generating the Hf-Nd mantle array. *Nature Geoscience* 1, 64–67.
- Chen, H.-L., Yang, S.-F., Wang, Q.-H., Luo, J.-C., Jia, C.-Z., Wei, G.-Q., Li, Z.-L., He, G.-Y., Hu, A.-P., 2006. Sedimentary response to the Early-Mid Permian basaltic magmatism in the Tarim plate. *Geology in China* 33, 545–552 (in Chinese with English abstract).
- Clemens, J.D., Holloway, J.R., White, A.J.R., 1986. Origin of an A-type granite: experimental constraints. *American Mineralogist* 71, 317–324.
- Collins, W.J., Beams, S.D., White, A.J.R., Chappell, B.W., 1982. Nature and origin of A-type granites with particular reference to southeastern Australia. *Contributions to Mineralogy and Petrology* 80, 189–200.
- Eby, G.N., 1990. The A-type granitoids: a review of their occurrence and chemical characteristics and speculations on their petrogenesis. *Lithos* 26, 115–134.
- Eby, G.N., 1992. Chemical subdivisions of the A-type granitoids: petrogenetic and tectonic implications. *Geology* 20, 641–644.
- Eby, G.N., 1998. Geochemistry and petrogenesis of nepheline syenite: Kasungu-Chipala, Ilomba, and Ulindi nepheline syenite intrusions, north Nyasa alkaline province, Malawi. *Journal of Petrology* 39, 1405–1424.
- Eugster, H.P., Wones, D.R., 1962. Stability relations of the ferruginous biotite, annite. *Journal of Petrology* 3, 82–125.
- Ferreira, V.P., Sial, A.N., Whitney, J.A., 1994. Large-scale silicate liquid immiscibility: a possible example from northeastern Brazil. *Lithos* 33, 285–302.
- Frost, C.D., Frost, B.R., 1997. Reduced rapakivi-type granites: the tholeiite connection. *Geology* 25, 647–650.
- Gao, Y.-S., 2007. Geological characteristics of Wajilitag vanadic titanomagnetite deposit and its prospecting recommendations. *Xinjiang Iron and Steel* 102, 8–9 (in Chinese).
- Gao, J.-F., Zhou, M.-F., Lightfoot, P.C., Wang, C.-Y., Qi, L., 2012. Origin of PGE-poor and Cu-rich magmatic sulfides from the Kalatongke deposit, Xinjiang, NW China. *Economic Geology* 107, 481–506.
- Ghiorso, M.S., Sack, R.O., 1995. Chemical mass transfer in magmatic processes IV: a revised and internally consistent thermodynamic model for the interpolation and extrapolation of liquid-solid equilibria in magmatic systems at elevated temperatures and pressures. *Contributions to Mineralogy and Petrology* 119, 197–212.
- Harney, D.M.W., von Gruenewaldt, G., 1995. Ore-forming processes of the upper part of the Bushveld complex, South Africa. *Journal of African Earth Science* 20, 77–89.
- Higgins, M.D., 2005. A new interpretation of the structure of the Sept-Iles intrusive suite, Canada. *Lithos* 83, 199–213.
- Hou, T., Zhang, Z.-C., Encarnacion, J., Santosh, M., 2012. Petrogenesis and metallogenesis of the Taihe gabbroic intrusion associated with Fe-Ti oxide ores in the Panxi district, Emeishan Large Igneous Province, southwest China. *Ore Geology Review* 49, 109–127.
- Huang, H., Zhang, Z.-C.K., Timothy, Santosh, M., Zhang, S., Zhang, D.-Y., Liu, J.-L., Zhao, Z.-D., 2012. Continental vertical growth in the transitional zone between South Tianshan and Tarim, western Xinjiang, NW China: insight from the Permian Halajun A1-type granitic magmatism. *Lithos*. doi:10.1016/j.lithos.2012.08.014.
- Huppert, H.E., Sparks, R.S.J., 1988. The generation of granitic magmas by intrusion of basalts into continental crust. *Journal of Petrology* 29, 599–624.
- Jia, C.-Z., 1997. Tectonic Characteristics and Petroleum, Tarim basin. Petroleum Industry Press, Beijing, China (in Chinese).
- Jiang, C.-Y., Zhang, P.-B., Lu, D.-R., Bai, K.-Y., 2004a. Source of the Fe-enriched-type high-Mg magma in Mazhartaig region, Xinjiang. *Acta Geologica Sinica* 78, 770–780 (in Chinese with English abstract).
- Jiang, C.-Y., Zhang, P.-B., Lu, D.-R., Bai, K.-Y., Wang, Y.-P., Tang, S.-H., Wang, J.-H., Yang, C., 2004b. Petrology, geochemistry and petrogenesis of the Kalpin basalts and their Nd, Sr and Pb isotopic compositions. *Geology Review* 50, 492–500 (in Chinese with English abstract).
- Jiang, C.-Y., Jia, C.-Z., Li, L.-C., Zhang, P.-B., Lu, D.-R., Bai, K.-Y., 2004c. Petrogenesis and magma source of the ultramafic rocks at Wajilitag region, western Tarim Plate in Xinjiang. *Acta Petrologica Sinica* 20, 1433–1444 (in Chinese with English abstract).
- Jiang, C.-Y., Li, Y.-Z., Zhang, P.-B., Ye, S.-F., 2006. Petrogenesis of Permian basalts on the western margin of the Tarim basin, China. *Russian Geology and Geophysics* 47, 237–248.
- Klemm, D.D., Henckel, J., Dehm, R., von Gruenewaldt, G., 1985. The geochemistry of titanomagnetite in magnetite layers and their host rocks of the eastern Bushveld Complex. *Economic Geology* 80, 1075–1088.
- Lepage, L.D., 2003. ILMAT: an Excel worksheet for ilmenite-magnetite geothermometry and geobarometry. *Computer Geoscience* 29, 673–678.
- Li, C.-N., Lu, F.-X., Chen, M.-H., 2001. Research on petrography of the Wajilitag complex body on the north edge of the Tarim Basin. *Xinjiang Geology* 19, 38–42 (in Chinese).
- Li, X.-H., Li, Z.-X., Zhou, H., Liu, Y., Kinny, P.D., 2002. U-Pb zircon geo-chronology, geochemistry and Nd isotopic study of the Neoproterozoic biomodal volcanic rocks in the Kangdian rift of South China: implication for the initial rifting of Rodinia. *Precambrian Research* 113, 135–154.
- Li, X.-H., Qi, C.-S., Liu, Y., Liang, X.-L., Tu, X.-L., Xie, L.-W., Yang, Y.-H., 2005. Rapid separation of Hf from rock samples for isotope analysis by MC-ICPMS: a modified single-column extraction chromatography method. *Geochemica* 34, 109–114 (in Chinese with English abstract).
- Li, X.-H., Li, Z.-X., Wingate, M.T.D., Chung, S.L., Liu, Y., Lin, G.-C., Li, W.-X., 2006. Geochemistry of the 755 Ma Mundine Well dyke swarm, northwestern Australia: part of a Neoproterozoic mantle superplume beneath Rodinia? *Precambrian Research* 146, 1–15.
- Li, Y.-Q., Li, Z.-L., Chen, H.-L., Yang, S.-F., Yu, X., 2012a. Mineral characteristics and metallogenesis of the Wajilitag layered mafic-ultramafic intrusion and associate d Fe-Ti-V oxide deposit in the Tarim large igneous province, northwest China. *Journal of Asian Earth Sciences* 49, 161–174.
- Li, Z.-L., Yang, S.-F., Chen, H.-L., Langmuir, C.-H., Yu, X., Lin, X.-B., Li, Y.-Q., 2008. Chronology and geochemistry of Taxinan basalts from the Tarim Basin: evidence for Permian plume magmatism. *Acta Petrologica Sinica* 24, 959–970 (in Chinese with English abstract).
- Li, Z.-L., Li, Y.-Q., Chen, H.-L., Santosh, M., Yang, S.-F., Xu, Y.-G., Langmuir, C.-H., Chen, Z.-X., Yu, X., Zou, S.-Y., 2012b. Hf isotopic characteristics of the Tarim Permian large igneous province rocks of NW China: Implication for the magmatic source and evolution. *Journal of Asian Earth Sciences* 49, 191–202.
- Lightfoot, P.C., Naldrett, A.J., Gorbachev, N.S., Fedorenko, V.A., Hawkesworth, C.J., Hergt, J., Doherty, W., 1994. Chemostratigraphy of Siberian Trap lavas, Noril'sk district, Russia: implications for the evolution of flood basalt magmas. *Ontario Geological Survey Special Volume* 5, 283–312.
- McCarthy, T.S., Cawthorn, R.G., Wright, C.J., Mylver, J.R., 1985. Mineral layering in the Bushveld Complex: implications of Cr abundances in magnetite from closely spaced magnetite and intervening silicate-rich layers. *Economic Geology* 80, 1062–1074.
- Naldrett, A.J., 2004. *Magmatic Sulfide Deposits: Geology, Geochemistry and Exploration*. Springer Verlag, Heidelberg, Germany.
- Namur, O., Charlier, B., Toplis, M.J., Higgins, M.D., Hounsell, V., Liégeois, J.P., Vander Auwer, J., 2011. Differentiation of tholeiitic basalt to A-type granite in the Sept-Iles layered intrusion, Canada. *Journal of Petrology* 52, 487–539.
- Nicholson, S.W., Cannon, W.F., Schulz, K.J., 1992. Metallogeny of the midcontinent rift system of North America. *Precambrian Research* 58, 355–386.
- Pang, K.-N., Li, C., Zhou, M.-F., Ripley, E.M., 2009. Mineral compositional constraints on petrogenesis and oxide ore genesis of the late Permian Panzhihua layered gabbroic intrusion, SW China. *Lithos* 110, 199–214.
- Pearce, J.A., Norry, M.J., 1979. Petrogenetic implications of Ti, Zr, Y, and Nb variations in volcanic rock. *Contributions to Mineralogy and Petrology* 69, 33–47.
- Peccerillo, A., Barberio, M.R., Yirgu, G., Ayalew, D., Barbieri, M., Wu, T.W., 2003. Relationships between mafic and peralkaline silicic magmatism in continental rift settings: a petrological, geochemical and isotopic study of the Gedessa Volcano, central Ethiopian rift. *Journal of Petrology* 44, 2003–2032.
- Pirajno, F., Ernst, R.E., Borisenko, A.S., Fedoseev, G., Naumov, E.A., 2009. Intraplute magmatism in Central Asia and China and associated metallogeny. *Ore Geology Review* 35, 114–136.
- Qin, K.-Z., Su, B.-X., Sakyi, P.A., Tang, D.-M., Li, X.-H., Sun, H., Xiao, Q.-H., Liu, P.-P., 2011. SIMS zircon U-Pb geochronology and Sr-Nd isotopes of Ni-Cu-bearing

- mafic-ultramafic intrusions in eastern Tianshan and Beishan in correlation with flood basalts in Tarim Basin (NW China): constraints on a ca. 280 Ma mantle plume. *American Journal of Science* 311, 237–260.
- Reynolds, I.M., 1985. Contrasted mineralogy and textural relationships in the uppermost titaniferous magnetite layers of the Bushveld Complex in the Bierkraal area north of Rustenburg. *Economic Geology* 80, 1027–1048.
- Roeder, P.L., Emslie, R.F., 1970. Olivine-liquid equilibrium. *Contributions to Mineralogy and Petrology* 29, 275–289.
- Rui, X.-J., He, J.-R., Guo, K.-Y., 2002. Mineral resources of Tarim Block (in Chinese). Geological Publishing House, Beijing (in Chinese with English abstract).
- Salter, V.J.M., 1996. The generation of mid-ocean ridge basalts from the Hf and Nd isotope perspective. *Earth and Planetary Science Letters* 141, 109–123.
- Schissel, D., Smail, R., 2001. Deep-mantle plumes and ore deposits. In: Ernst, R.E., and Buchan, K.L. (Eds.), *Mantle Plumes: Their Identification Through Time*. Geological Society of America Special Paper 352, pp. 291–322.
- Shellnutt, J.G., Zhou, M.-F., 2007. Permian peralkaline, peraluminous and metallocious A-type granites in the Panxi district, SW China: their relationship to the Emeishan mantle plume. *Chemical Geology* 242, 286–316.
- Shellnutt, J.G., Wang, C.-Y., Zhou, M.-F., Yang, Y.-H., 2009. Zircon Lu-Hf isotopic compositions of metallocious and peralkaline A-type granitic plutons of the Emeishan large igneous province (SW China): constrain ts on the mantle source. *Journal of Asian Earth Sciences* 35, 45–55.
- Stormer Jr, J.C., 1983. The effects of recalculation on estimates of temperature and oxygen fugacity from analyses of multi-component iron-titanium oxides. *American Mineralogist* 68, 586–594.
- Sun, S.S., McDonough, W.F., 1989. Chemical and isotopic systematics of oceanic basalts: implications for mantle composition and processes. In: Saunders, A.D., Norry, M.J. (Eds.), *Magmatism in the Ocean Basins*. Geological Society London Special Publications.
- Tian, W., Campbell, I.H., Allen, C.M., Guan, P., Pan, W.-Q., Chen, M.-M., Yu, H.-J., Zhu, W.-P., 2010. The Tarim picrite–basalt–rhyolite suite, a Permian flood basalt from northwest China with contrasting rhyolites produced by fractional crystallization and anatexis. *Contributions to Mineralogy and Petrology* 160, 407–425.
- Toplis, M.J., Carroll, M.R., 1995. An experimental study of the influence of oxygen fugacity on Fe-Ti oxide stability, phase relations, and mineral-melt equilibria in ferrobasaltic systems. *Journal of Petrology* 36, 1137–1170.
- Toplis, M.J., Corgne, A., 2002. An experimental study of element partitioning between magnetite, clinopyroxene and iron-bearing silicate liquids with particular emphasis on vanadium. *Contributions to Mineralogy and Petrology* 144, 22–37.
- VanTongeren, J.A., Mathez, E.A., 2012. Large-scale liquid immiscibility at the top of the Bushveld Complex, South Africa. *Geology* 40, 491–494.
- Veksler, I.V., Dorfman, A.M., Borisov, A.A., Wirth, R., Dingwell, D.B., 2007. Liquid immiscibility and the evolution of basaltic magma. *Journal of Petrology* 48, 2187–2210.
- Vincent, E.A., Phillips, R., 1954. Iron titanium oxide minerals in layered gabbros of Skaergaard intrusion, East Greenland. *Geochimica Cosmochimica Acta* 6, 1–26.
- von Gruenewaldt, G., 1993. Ilmenite-apatite enrichments in the Upper Zone of the Bushveld Complex: a major titanium-rock phosphate resource. *International Geology Review* 35, 987–1000.
- von Gruenewaldt, G., Klemm, D.D., Henckel, J., Dehm, R.M., 1985. Exsolution features in titanomagnetites from massive magnetite layers and their host rocks of the Upper Zone, eastern Bushveld Complex. *Economic Geology* 80, 1049–1061.
- Wager, L.R., Brown, G.M., 1968. *Layered Igneous Rock*. Edinburgh.
- Wang, C.-Y., Zhou, M.-F., 2013. New textural and mineralogical constraints on the origin of the Hongge Fe-Ti-V oxide deposit, SW China. *Mineralium Deposita*. <http://dx.doi.org/10.1007/s00126-013-0457-4>.
- Wei, X., Xu, Y.-G., 2011. Petrogenesis of Xiaohaizi syenite complex from Bachu area, Tarim. *Acta Petrologica Sinica* 27, 2984–3004 (in Chinese with English abstract).
- Wei, X., Xu, Y.-G., Feng, X.-Y., Zhao, J.-X., 2013. Plume-lithosphere interaction in the generation of the Tarim large igneous province, NW China: geochronological and geochemical constraints. *American Journal of Sciences* (revised ms).
- Weibe, R.A., 1996. Mafic-silicic layered intrusions: the role of basaltic injections on magmatic processes and the evolution of silicic magma chambers. *Transactions of the Royal Society of Edinburgh: Earth Sciences* 87, 233–242.
- Weaver, B.L., 1990. Geochemistry of highly-undersaturated ocean island basalt suites from the South Atlantic Ocean: Fernando de Noronha and Trinidad islands. *Contributions to Mineralogy and Petrology* 105, 502–515.
- Wilson, M., 1989. Igneous Petrogenesis. Unwin Hyman, London, pp. 245–285.
- Xinjiang Bureau of Geology and Mineral Resources, 1993. Regional geology of the Xinjiang Uygur Autonomous Region. Geology Publishing House, Beijing (in Chinese).
- Xu, Y.-G., He, B., Luo, Z.-Y., Liu, H.-Q., 2013. Study on Mantle Plume and Large Igneous Provinces in China: An Overview and Perspectives. *Bulletin of Mineralogy Petrology and Geochemistry* 32, 25–39 (in Chinese with English abstract).
- Yang, S.-F., Chen, H.-L., Dong, C.-W., Jia, C.-Z., Wang, Z.-G., 1996. The discovery of Permian syenite inside Tarim basin and its geodynamic significance. *Geochemistry* 25, 121–128 (in Chinese with English abstract).
- Yang, S.-F., Chen, H.-L., Dong, C.-W., Jia, C.-Z., Wei, G.-Q., Wang, Z.-G., 1997. Geological thermal event of Tarim basin. *Chinese Science Bulletin* 42, 1096–1099 (in Chinese with English abstract).
- Yang, S.-F., Chen, H.-L., Ji, D.-W., Li, Z.-L., Dong, C.-W., Jia, C.-Z., Wei, G.-Q., 2005. Geological process of early to middle Permian magmatism in Tarim basin and its geodynamic significance. *Geological Journal of China Universities* 11, 504–511 (in Chinese with English abstract).
- Yang, S.-F., Li, Z.-L., Chen, H.-L., Xiao, W.-J., Yu, X., Lin, X.-B., Shi, X.-G., 2006. Discovery of a Permian quartz syenitic porphyritic dyke from the Tarim Basin and its tectonic implications. *Acta Petrologica Sinica* 22, 1405–1412 (in Chinese with English abstract).
- Yang, S.-F., Li, Z.-L., Chen, H.-L., Santosh, M., Dong, C.-W., Yu, X., 2007. Permian bimodal dyke of Tarim Basin, NW China: geochemical characteristics and tectonic implications. *Gondwana Research* 12, 113–120.
- Yu, X., Yang, S.-F., Chen, H.-L., Chen, Z.-Q., Li, Z.-L., Li, Y.-Q., 2011. Permian flood basalts from Tarim Basin, Northwest China: SHRIMP zircon U-Pb dating and geochemical characterizations. *Gondwana Research* 20, 485–497.
- Zhang, C.-L., Li, X.-H., Li, Z.-X., Ye, H.-M., Li, C.-N., 2008. A Permian layered intrusive complex in the Western Tarim Block, Northwestern China: product of a Ca. 275 Ma mantle plume? *Journal of Geology* 116, 269–287.
- Zhang, C.-L., Xu, Y.-G., Li, Z.-X., Wang, H.-Y., Ye, H.-M., 2010a. Diverse Permian magmatism in the Tarim Block, NW China: genetically linked to the Permian Tarim mantle plume? *Lithos* 119, 537–552.
- Zhang, C.-L., Li, Z.-X., Li, X.-H., Xu, Y.-G., Zhou, G., Ye, H.-M., 2010b. A Permian large igneous province in Tarim and Central Asian orogenic belt, NW China: results of a ca. 275 Ma mantle plume? *Geological Society of America Bulletin* 122, 2020–2040.
- Zhang, Y.-T., Liu, J.-Q., Guo, Z.-F., 2010c. Permian basaltic rocks in the Tarim basin NW China: implications for plume–lithosphere interaction. *Gondwana Research* 18, 596–610.
- Zhou, M.-F., Robinson, P.T., Lesher, C.M., Keays, R.R., Zhang, C.-J., Malpas, J., 2005. Geochemistry, petrogenesis and metallogenesis of the Panzhihua gabbroic layered intrusion and associated Fe-Ti-V oxide deposits, Sichuan Province, SW China. *Journal of Petrology* 46, 2253–2280.
- Zhou, M.-F., Arndt, N.T., Malpas, J., Wang, C.-Y., Kennedy, A.K., 2008. Two magma series and associated ore deposit types in the Permian Emeishan large igneous province, SW China. *Lithos* 103, 352–368.
- Zhou, M.-F., Zhao, J.-H., Jiang, C.-Y., Gao, J.-F., Wang, W., Yang, S.-H., 2009. OIB-like, heterogeneous mantle sources of Permian basaltic magmatism in the western Tarim Basin, NW China: implications for a possible Permian large igneous province. *Lithos* 113, 583–594.
- Zhong, H., Zhu, W.-G., Chu, Z.-Y., He, D.-F., Song, X.-Y., 2007. SHRIMP U-Pb zircon geochronology, geochemistry, and Nd-Sr isotopic study of contrasting granites in the Emeishan large igneous province, SW China. *Chemical Geology* 236, 112–133.
- Zhong, H., Zhu, W.-G., Hu, R.-Z., Xie, L.-W., He, D.-F., Liu, F., Chu, Z.-Y., 2009. Zircon U-Pb age and Sr-Nd-Hf isotope geochemistry of the Panzhihua A-type syenitic intrusion in the Emeishan large igneous province, southwest China and implications for growth of juvenile crust. *Lithos* 110, 109–128.